



OPEN Stability and control mechanism of nonlinear horizontal vibration for rolling system with gyroscope precession effect

Chaofan Sun^{1,2}✉, Wu Zhao³, Wei Liu^{1,2}, Guiquan Han^{1,2}, Yuqi Chen^{1,2} & Junyang Duan⁴

This paper investigates the nonlinear horizontal vibration of a cold rolling system induced by the gyroscope precession effect—a critical yet underexplored issue affecting strip quality and rolling stability. A nonlinear dynamic model is developed by incorporating the axial excitation force and the elastic deformation of the work roll based on d'Alembert principles. The primary parametric resonance response, corresponding to the first Arnold tongue, is analyzed using the multi-scale method and validated experimentally. To further understand the systematic dynamic behavior, the homotopy analysis method is employed to trace the evolution of energy orbits, revealing bifurcation and jump phenomena as the frequency ratio varies. A devil's staircase pattern emerges, indicating multiple frequency-locked regions. These nonlinear features are further validated through cell mapping techniques, which depict the transformation of modal energy manifolds. Moreover, by introducing active control inputs, a constraint space for control parameters is designed to induce amplitude death within the maximum Arnold tongue region. The findings contribute to a deeper understanding of the resonance mechanism and offer a theoretical basis for stabilizing precision cold rolling systems via nonlinear control strategies.

Keywords Rolling mill, Horizontal vibration, Homotopy analysis, Cell mapping theory, Amplitude death

List of symbols

X, Y, Z	Fixed space coordinates (/)
θ	Angle between the projections of the axial lines of backup and work roll onto the XY plane (rad)
r_1	Work roll radius (mm)
r_2	Backup roll radius (mm)
α	Angle between the connection line of the centers of the backup roll and work roll and the Z-axis (rad)
c	Equivalent damping coefficient (N s/m)
k	Equivalent stiffness coefficient (N/m)
e	Eccentricity (mm)
Q	Reduction force (N)
P	Rolling force (N)
μ	Friction coefficient between rolls (/)
V_B	Linear velocities on backup rolls' surfaces (m/s)
V_W	Linear velocities on work rolls' surfaces (m/s)
V_{BW}	Relative speed vector (m/s)
F_1^p	Axial force acting on the axis direction of work roll (N)
F_{11}^p	Surface-contacting frictions respectively normal to the central lines of work roll (N)
F_{12}^p	Surface-contacting frictions respectively normal to the central lines of backup roll (N)
ω	Excitation angular frequency (rad/s)
Ω	Angular speed (rad/s)
ψ	Slopes of bending deformation at X directions (/)

¹School of Intelligent Manufacturing and Electrical Engineering, Nanyang Normal University, Nanyang 473061, China. ²Collaborative Innovation Center of Intelligent Explosion-Proof Equipment, Nanyang, Henan Province, China. ³School of Mechanical and Power Engineering, Henan Polytechnic University, Jiaozuo 454003, China. ⁴Jinguan Electric Co., Ltd, Nanyang 473003, China. ✉email: sunchaofanxw@163.com

ϕ	Slopes of bending deformation at Z directions (l)
ρ	Density per unit length of the work roll (kg/m^4)
A	Cross-sectional area of work roll (mm^2)
I	Inertia moment (mm^4)
E_1	Elastic modulus of work roll (Pa)
m	Mass per unit length of work roll (kg/m)
M	Bending moment (N m)
q	Shear force (N)
κ	Shear coefficient of work roll (l)
G	Shear modulus of work roll (Pa)
u	Deflection of work roll at X direction (mm)
w	Deflection of work roll at Z direction (mm)
σ	Stress (Pa)
l	Length of work roll (mm)
l_0	Projection of l at the y direction (mm)
ω_0	Inherent frequency of work roll (rad/s)
k_1	Parameter-stimulating stiffness coefficient (l)
k_3	Nonlinear stiffness coefficient (l)
g_1	Displacement gain (mm)
g_2	Velocity gain (mm/s)
t_d	Time delay (s)
T_0	Fast time scales (s)
T_1	Slow time scales (s)
η	Small parameter (l)
D_n^m	The m th order partial derivative of the n th time scale (l)
cc	Conjugate term (mm)
ST_1	Duration term (mm)
\tilde{h}	Nonzero auxiliary parameter (l)
$H(t)$	Auxiliary function (l)
V	Phase volume (l)
M_0	Original set (l)
M_r	Set (l)
D	Phase space (l)
Σ_0	Poincaré section (l)
Γ	Phase trajectory (l)

Cold rolled thin sheets, as an extremely important product in the steel rolling industry, are widely used in precision manufacturing fields such as rail transit, electronic information, aerospace, automotive and aircraft skins. The precision of cold rolling forming of thin sheets heavily depends on the working accuracy of the rolling mill structure and the rolling stability. With the continuous improvement in the quality requirements for cold-rolled thin sheet products, nonlinear vibration problems in mill equipment and their impact on thin plate quality have received increasing attention. An in-depth study of the nonlinear vibration mechanism and stability of rolling mills is of great significance to improve the high-quality development of downstream industries such as the above-mentioned high-precision manufacturing fields with cold rolled thin plates as raw materials¹.

At present, despite extensive research on nonlinear vibration in rolling systems, most existing studies have focused on vertical^{2–4} or torsional^{5–7} vibrations, while horizontal vibrations—especially those induced by gyroscope precession effects—remain underexplored. However, the horizontal vibration phenomenon of rolling mill equipment in the domestic and foreign steel rolling industry frequently occurs, which poses significant risks. Firstly, horizontal vibrations directly affect the lateral stability and uniformity of the rolling gap, which is critical for strip shape control and edge straightness. Even small horizontal displacements can lead to asymmetrical deformation, especially in thin strip rolling. Secondly, compared to vertical vibration, horizontal vibrations are more sensitive to mechanical imperfections such as bearing clearance, misalignment, and assembly-induced eccentricities, which can cause complex vibration behaviors that are hard to detect and control. The micro-scale behavior induced by these defects in horizontal vibration is usually more difficult to model and suppress. In addition, horizontal vibration also causes alternating light and dark vibration patterns on the surface of rolls and rolled parts. In severe cases, it can also lead to accidents such as strip breakage, steel stacking, and roll shifting⁸. These issues are primarily triggered by micro-scale behaviors arising from unavoidable assembly clearances and roll misalignments, which introduce complex nonlinear dynamics. Therefore, there is a strong industrial and academic demand to develop a comprehensive analytical model that captures these micro-scale effects and provides an effective control strategy for horizontal vibration suppression. This paper addresses this gap by establishing a nonlinear dynamic model of work roll horizontal vibration under axial excitation, analyzing its bifurcation and energy evolution characteristics, and proposing a delay-feedback control mechanism to mitigate the associated resonance and instability.

In rolling production, due to the existence of inevitable errors such as the gap between the roll neck and the bearing pedestal, as well as the inevitable error between the bearing pedestal and frame due to manufacturing, installation, wear and other factors⁹, the combined effects of gyroscope precession and eccentricity between the rolls are generated, which induce serious nonlinear horizontal vibrations in the roll system¹⁰, severely restricting the surface quality of rolled products and the online service life of the roll system. It is a problem that needs to be solved urgently in the steel rolling industry at present^{11,12}.

In recent years, the domestic and foreign research work on the rolling process is mainly based on the Karman and Orowan equations. Under different research hypotheses, the vibration characteristics under the influence of factors such as frictional force at the rolling interface and elastic-plastic deformation of the rolled piece have been studied. By analyzing the effects of various nonlinear factors such as dynamic changes of rolling force¹³, horizontal vibration of rolling pieces^{14,15}, it is found that there are abundant nonlinear phenomena in the horizontal direction, such as bifurcations and chaotic motions. Jiang et al.^{16,17} and Cui et al.¹⁸ developed fractional-order nonlinear vibration models of horizontal roll systems, revealing the influence of system parameters and fractional orders on sub-/super-harmonic resonances and bifurcations, and validated the effectiveness of feedback controllers in suppressing phenomena such as jump and hysteresis.

Zhou¹⁹ established the roll's nonlinear horizontal forced vibration model considering factors such as nonlinear damping and installation error gaps, and the results indicate that the horizontal vibration phenomenon of the lower work roll is most sensitive to tension fluctuations. Zhao et al.^{20,21} investigated the systematic chatter by the coupling with dynamic rolling model and mill structural model. The stable parameter domain for rolling processing is obtained, and it is determined that work roll prioritizes horizontal vibration while backup roll prioritizes vertical vibration. Li et al.²² investigated the amplitude-frequency response characteristics of nonlinear horizontal vibration of rolling mills by the multi-scale method, and found that the jump phenomenon and the unstable region can be adjusted by changing the nonlinear stiffness as well as the damping values, which is helpful for suppressing the horizontal vibration. Liu²³, considering the interaction between the rolling mill structure and the vibration of the rolled piece, established a dynamic equilibrium equation along the rolling direction. Using the multi-scale method to analyze the systematic amplitude-frequency characteristics, it was found that with changes in the external excitation frequency, the system amplitude exhibited significant jump phenomena. However, although the above literature has conducted sufficient research on the nonlinear dynamic behavior and rolling stability of horizontal vibration under the influence of assembly clearance, structural parameters, and excitation frequency, there are few in-depth studies on the internal mechanism of system vibration characteristics and stability under the influence of roll's gyroscope precession.

Based on the above research, relevant scholars have further studied the boundary conditions of micro-scale behavior caused by gap errors. Shen and Li^{24,25} confirmed that out of control of rolls' position would give rise to the static intersection between rolls and yield big axial force which would induce the horizontal nonlinear vibration on rolls. Fan et al.²⁶ conducted on-site measurements on the clearance of the rolling mill frame and found that eliminating the bearing clearance of the rolling mill frame can effectively suppress the roll's nonlinear horizontal vibration. As the reduction rate and clearance increase, the axial force generated by the cross-section of the rolling mill increases, on the contrary, if increasing the clearance and reduction rate, the axial force originated on roll's section would get enlarged, whose influence on the system cannot be ignored. Considering the influence of the clearance between roll's bearing pedestal and mill frame, Zheng et al.²⁷ investigated the vibration mode in three-dimension dynamic system. The results indicate the structural clearance can raise the structural instability with low frequency. The vibration measurement on site shows the vibration is the combination of horizontal and vertical ones, where the second and fourth combined modes are mainly horizontal, while the third is predominantly vertical. To address dynamic instabilities under structural complexities, Sun et al.²⁸ incorporated gyroscope precession and eccentricity effects into a nonlinear vibration model and applied bifurcation and cell mapping techniques to identify chaotic regimes. Complementing these efforts, He et al.²⁹ introduced an intelligent hydraulic liner based on a fractional-order model, offering a practical solution for mitigating horizontal nonlinear vibrations. Chen et al.³⁰ developed a robust, low-complexity control strategy for decoupled vibration subsystems, achieving strong disturbance rejection and ensuring stable mill operation under uncertainties. Nevertheless, relatively few studies have addressed horizontal vibrations caused specifically by gyroscope precession effects and their impact on system stability and control. This motivates the present work, which aims to fill this gap through dynamic modeling, modal energy analysis, and control strategy design based on amplitude death theory.

By comparing the above domestic and international research on the nonlinear vibrations of asynchronous cold rolling systems, it is found that it is difficult to achieve consistent conclusions in terms of specific guiding results. This may be due to the neglect of the impact of random vibration phenomena induced by micro-scale behaviors during the research process, primarily manifested as horizontal vibrations caused by structural gap errors in the rolling mill. To address the issue that vibration phenomena induced by nonlinear factors in the current rolling system make it difficult to further improve rolling stability, this paper takes a four-high cold rolling mill as the research object and considers factors such as structural clearance errors that are often blurred or ignored, such as the gyroscope effect caused by the micro gap between the roll neck and the bearing pedestal. The nonlinear dynamic model of the horizontal vibration for the working roll is established. Unlike previous research, this paper focuses on exploring the systematic stability in an unstable state, specifically analyzing the amplitude-frequency characteristics of primary parametric resonance corresponding to the maximum Arnold tongue. Furthermore, the homotopy analysis method is used to analyze the energy orbit evolution curves of various modal amplitudes in the work roll horizontal vibration system. Secondly, using multiple locked frequency regions with devil's staircase patterns in the energy orbit evolution curves as entry points, a cell mapping approach is employed to depict the manifold changes in the energy of oscillator groups, verifying the modal energy orbit evolution characteristics in the steady-state response. Finally, introducing the active control signal, the set of control parameter constraints is constructed to achieve the systematic amplitude death state under the influence of the gyroscopic effect. The theoretical research results mentioned above will establish the mutation mechanism and stability theory of horizontal vibrations in a four-high cold rolling system. This provides theoretical references for suppressing and controlling nonlinear horizontal vibrations in the roll system under gyroscopic effects, ultimately improving the quality of rolled sheets.

Problem formulation and structural modeling Institutional incentives for roll's horizontal vibration

During the rolling process on a four-high cold mill, the bearing pedestals of the lower backup roll and lower work roll are fixed in place. The mill's pressing mechanism generates a rolling force that is applied to the bearing housing of the upper backup roll. Subsequently, the upper backup roll is driven into contact with the rotating upper work roll, where circumferential load transfer occurs. Finally, the workpiece undergoes plastic deformation within the clearance between the two work rolls, which rotate relative to each other. To eliminate the horizontal structural gaps between the bearing pedestal and the frame rail—caused by mechanical variations during the rolling process¹⁰—and to improve rolling stability, the work roll is intentionally offset and installed relative to the centerline of the backup roll. This arrangement helps prevent rolling instability due to nonlinear vibrations induced by structural gaps.

However, for a high-speed precision four-high cold mill, the inevitable gap between the roll neck and its corresponding bearing pedestal cannot be ignored. This gap is further amplified by deformation caused by rolling pressure, causing the two rolls—originally intended to be centered—to intersect in the horizontal plane, as illustrated in Fig. 1. Figure 1b shows the top view corresponding to Fig. 1a.

In fixed coordinates XYZ in Fig. 1 X is for the horizontal motion direction of the rolls, Y is for the axial direction and Z is for the vertical direction. α is the angle between the center connection line of backup roll and work roll caused by the offset setting and the Z-axis. r_1 and r_2 are the radii of the work roll and backup roll

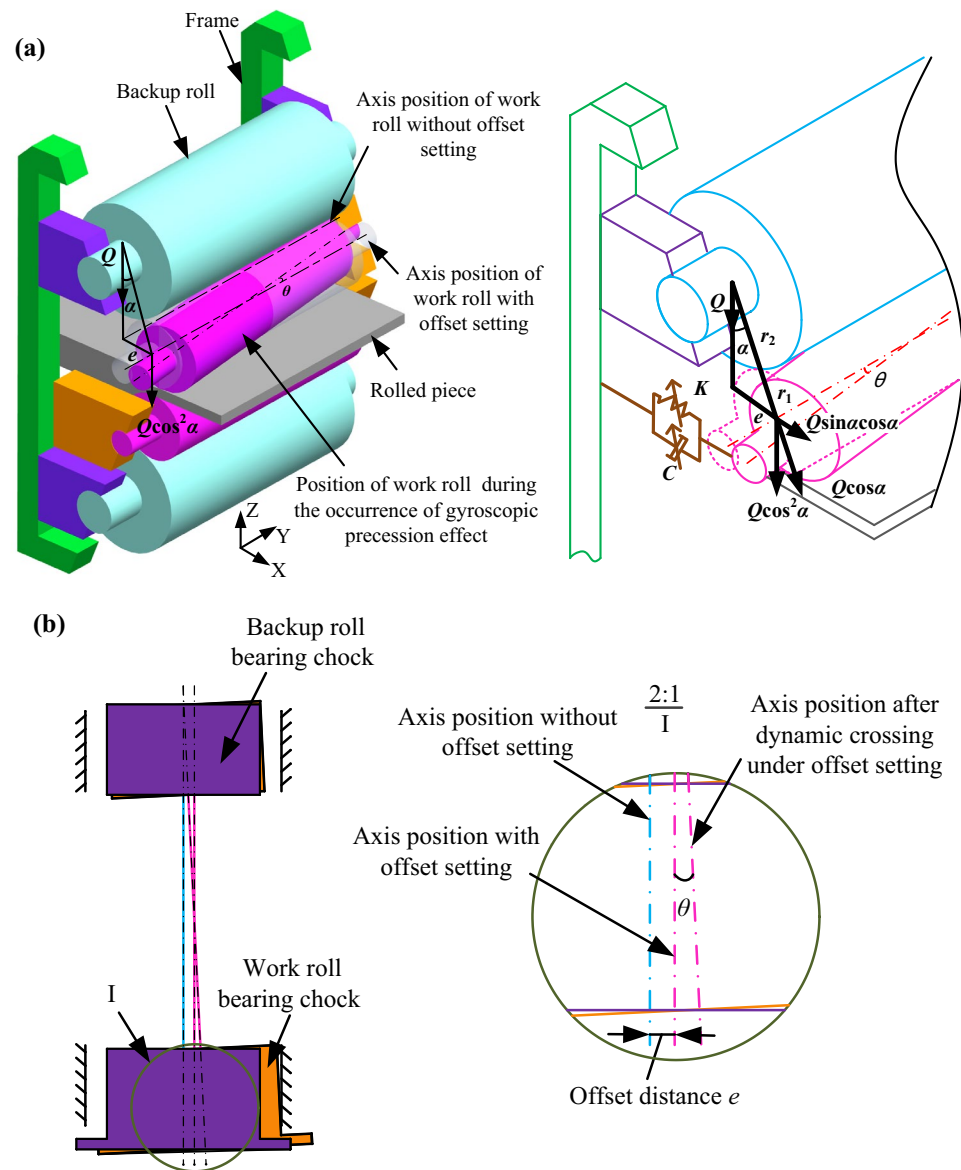


Fig. 1. Mechanism model of work roll horizontal vibration in four-high mill. The 3D image was created using SolidWorks 2016 (Dassault Systèmes, <https://www.solidworks.com>).

respectively. k and c represent the equivalent stiffness and damping coefficients, respectively, in the horizontal direction of the work roll. Q represents the reduction force exerted by the mill screwdown system on the bearing chock of backup roll. At this moment, the force exerted by the backup roll on the work roll is $Q\cos\alpha$, whose vertical component along the Z axis is $Q\cos^2\alpha$. The horizontal component along the X -axis, $Q\sin\alpha\cos\alpha$, cancels out with the reactive force from the frame on the bearing pedestal, as shown in Fig. 1a. θ is for the intersectional angle between backup and work rolls in XY plane, and e is for the eccentricity in the horizontal direction between central lines of the two rolls, shown in Fig. 1b. According to the structural errors and force geometry shown in Fig. 1, it is known that due to the force $Q\cos\alpha$, angle θ would induce the contact friction between roll surfaces and yield the gyroscope precession of backup roll to work roll, and finally produce the axial component imposing on the work roll. The effect of the above force causes micro-vibrations of the work roll in the horizontal direction^{25,26}, which can undermine the stability of the work roll in the same direction.

Nonlinear horizontal vibration model of work roll under gyroscope precession effect

The force exerted by the backup roll on the work roll is $Q\cos\alpha$. Its vertical component, $Q\cos^2\alpha$, is assumed to be equal to the rolling force P exerted by the work roll on the workpiece. As described above, in the case where the axial lines of the rolls intersect, the rolls’ relative rotation would generate spiral precession due to friction contact under the force $Q\cos\alpha$, which can induce an additional axial force FP 1, as shown in Fig. 2. Under this axial force, roll would output the vertical and horizontal vibrations. Combining with the institutional characteristics and operation processing of four-high cold rolling system, the horizontal vibration model is constituted induced by rolling force in cold mill system. Based on the model, the evolution mechanism of the work roll’s horizontal vibration from instability to transient equilibrium, and then to stability is analyzed. The premises for the model constitution are as follows:

- (1) The backup and work rolls keep level in horizontal plane, and there is no pitch angle in axial direction;
- (2) The backup roll has no skew angle in the horizontal plane, while the work roll has a cross angle with the backup roll in the horizontal plane, taken as θ .

The gyro model resulting from friction contact between backup and work rolls is illustrated in Fig. 2. V_B and V_W are for the linear velocities of backup and work rolls’ surfaces respectively, V_{BW} on the surface is for the relative velocity vector. Once imposing force $Q\cos\alpha$, friction stress occurs between the roll surfaces, FP 11 and FP 12 represent for the surface-contacting frictions respectively normal to the central lines of work and backup rolls, which just drive the backup roll to move in spiral with respect to work roll, and the generated axial force FP 1 acting on the backup roll is in the same direction as V_{BW} . If only taking into account for the axial force caused by the rolls’ intersection, and assuming the axial forces loading on work and backup rolls are approximate, according to the forces balance law on roll’s surfaces, in terms of literature²⁵, the axial force can be expressed as

$$F_1^P = \mu(Q \cos \alpha \cos \omega \bar{t}) \sin \theta = \frac{\mu (P \cos \omega \bar{t}) \sin \theta}{\cos \alpha} \tag{1}$$

where μ is for the coefficient of friction between rolls, and ω is for the exciting angular frequency of force. The work roll keeps in rotation all way during rolling processing, where there exist shear deformation and the inertial moment on sectional area around the neutral axis. In order to facilitate analysis, take the work roll as the equivalent Timoshenko beam with ends fixed-hinge support³¹⁻³³. According to the stress state of the work roll, the loaded periodic axial force is FP 1, as shown in Fig. 3, where $u(Y, \bar{t})$ and $w(Y, \bar{t})$ are the absolute

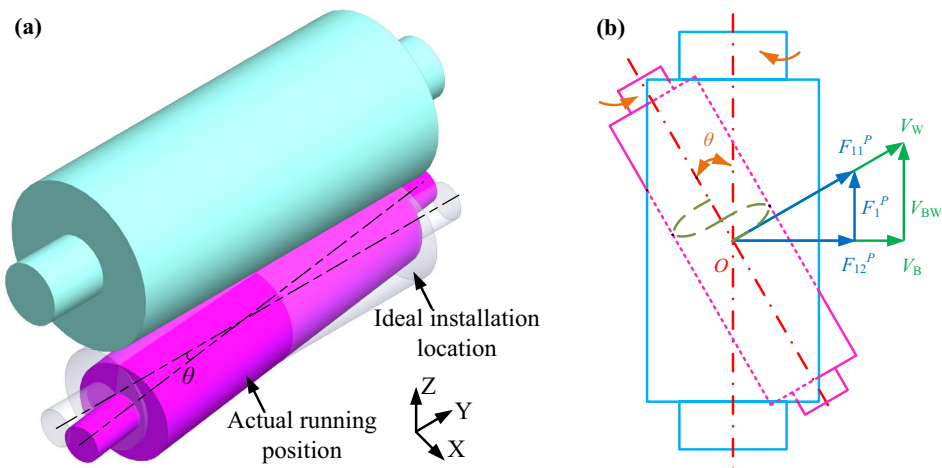


Fig. 2. Schematic diagram of rolls cross. The 3D image was created using SolidWorks 2016 (Dassault Systèmes, <https://www.solidworks.com>).

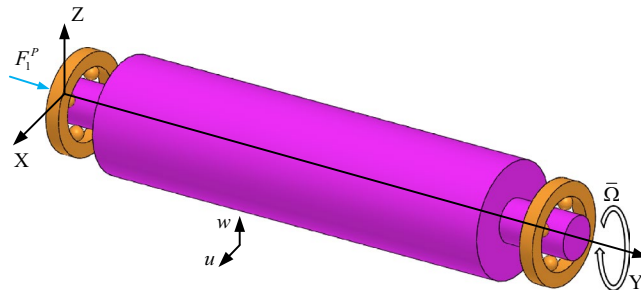


Fig. 3. Schematic diagram of the equivalent simply-supported beam loaded by axial and lateral force. The 3D image was created using SolidWorks 2016 (Dassault Systèmes, <https://www.solidworks.com>).

displacements in the coordinate system XYZ. The work roll rotates around the axis (Y-axis) at a constant angular speed $\bar{\Omega}$.

The rotation angle vector of the work roll can be expressed as³⁴

$$\vec{\omega} = \bar{\Omega} \cos \phi \cos \psi \vec{i} + \left(-\frac{\partial \phi}{\partial t} + \bar{\Omega} \cos \phi \sin \psi \right) \vec{j} + \left(-\frac{\partial \psi}{\partial t} + \bar{\Omega} \sin \phi \right) \vec{k} \tag{2}$$

where $\psi = \partial u(Y, \bar{t}) / \partial Y$ and $\phi = \partial w(Y, \bar{t}) / \partial Y$ are the slopes of bending deformation in X and Z directions respectively. Assuming the roll has small deformation, Eq. (2) is further simplified as

$$\vec{\omega} = \bar{\Omega} \vec{i} + \left(-\frac{\partial \phi}{\partial t} + \bar{\Omega} \psi \right) \vec{j} + \left(-\frac{\partial \psi}{\partial t} + \bar{\Omega} \phi \right) \vec{k} \tag{3}$$

The roll's total kinetic energy can be expressed as

$$T = \frac{1}{2} \int_0^l \left\{ \rho A \left[\left(\frac{\partial u}{\partial \bar{t}} \right)^2 + \left(\frac{\partial w}{\partial \bar{t}} \right)^2 \right] + \rho I \left[2\bar{\Omega}^2 + \left(-\frac{\partial \phi}{\partial t} + \bar{\Omega} \psi \right)^2 + \left(-\frac{\partial \psi}{\partial t} + \bar{\Omega} \phi \right)^2 \right] \right\} dY \tag{4}$$

where roll's density is ρ , sectional area is A , and I is the inertia moment. On the other hand, the roll's potential energy is

$$U = \frac{1}{2} \int_0^l \left\{ E_1 I \left[\left(\frac{\partial^2 u}{\partial Y^2} \right)^2 + \left(\frac{\partial^2 w}{\partial Y^2} \right)^2 \right] + F_1^P \left[\left(\frac{\partial u}{\partial Y} \right)^2 + \left(\frac{\partial w}{\partial Y} \right)^2 \right] \right\} dY \tag{5}$$

where E_1 is the roll's elastic modulus, the first part of the integral is the bending potential energy and the second part is the axial deformation potential energy.

Hamilton principle is

$$\delta \int_{t_1}^{t_2} (T - U) d\bar{t} = 0 \tag{6}$$

The single horizontal displacement $u(Y, \bar{t})$ of the roll is analyzed, assuming that the roll's material is isotropic and linear elastic. Figure 4 shows the deformation movement of the roll's microelement. It not only bears pure bending deformation, but also shear deformation. The stress state of the microelement with the length of dY on the roll is analyzed.

Let the roll microelement dY bend slightly due to deformation, and the angle between both ends and Y-axis is ψ and ψ' , the axial force is N and N' respectively, shear force is q and q' , the bending moment is M and M' . The above parameters meet the following relations

$$\psi' = \psi + \frac{\partial \psi}{\partial Y} dY, N' = N + \frac{\partial N}{\partial Y} dY, q' = q + \frac{\partial q}{\partial Y} dY, M' = M + \frac{\partial M}{\partial Y} dY \tag{7}$$

Considering the influence of the roll's main shear deformation, the horizontal balance equation of the work roll microelement is obtained from the d'Alembert principle as follows

$$-m \frac{\partial^2 u}{\partial \bar{t}^2} dY - c \frac{\partial u}{\partial \bar{t}} dY - q + q' + \rho I \left(1 + \frac{E_1}{\kappa G} \right) \frac{\partial^4 u}{\partial Y^2 \partial \bar{t}^2} dY + N \sin \psi - N' \sin \psi' = 0 \tag{8}$$

where m and c are the mass and damping coefficient per unit length respectively; κ is the shear coefficient and G is the shear modulus.

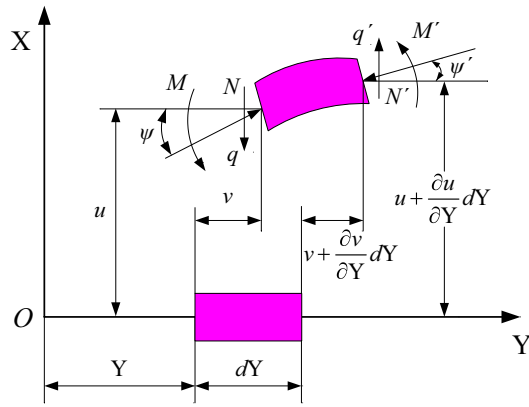


Fig. 4. Force state of the micro-element for work roll.

Substituting Eqs. (7) into (8), we get

$$-m \frac{\partial^2 u}{\partial t^2} - c \frac{\partial u}{\partial t} + \rho I \left(1 + \frac{E_1}{\kappa G} \right) \frac{\partial^4 u}{\partial Y^2 \partial t^2} + \frac{\partial q}{\partial Y} - N \frac{\partial^2 u}{\partial Y^2} - \frac{\partial N \sin \psi}{\partial Y} = 0 \tag{9}$$

According to the moment balance of the roll microelement

$$q = \frac{\partial M}{\partial Y}, \quad M = -E_1 I \frac{\partial \psi}{\partial Y}, \quad \psi = \frac{\partial u}{\partial Y} \tag{10}$$

From Eqs. (9) and (10), substituting T and U into Hamilton system, thus we have

$$m \frac{\partial^2 u}{\partial t^2} + c \frac{\partial u}{\partial t} + E_1 I \frac{\partial^4 u}{\partial Y^4} - \rho I \left(1 + \frac{E_1}{\kappa G} \right) \frac{\partial^4 u}{\partial Y^2 \partial t^2} + N \frac{\partial^2 u}{\partial Y^2} + \sin \psi \frac{\partial N}{\partial Y} - \rho I \bar{\Omega}^2 \frac{\partial^2 u}{\partial Y^2} = 0 \tag{11}$$

Assume that the axial force acting on the work roll is uniformly distributed, so N is independent of Y , that is, $\partial N / \partial Y = 0$. Furthermore, due to the roll deformation, the axial force in its cross section is no longer the axial force generated by the gyroscope precession, but also includes the additional force caused by the axial shortening of the microelement segment due to the work roll's lateral displacement, so the axial force has the following form

$$N = F_1^P - \sigma A \tag{12}$$

where σ is stress.

Assume that the roll's length does not change after bending deformation, the deflection curve equation is $u = u(Y, \bar{t})$, the projection in the Y direction is l_0 , and the microelement of its axis curve is taken

$$\Delta s = \sqrt{(\Delta Y)^2 + (\Delta u)^2} = \Delta Y \sqrt{1 + \left(\frac{\partial u}{\partial Y} \right)^2} \tag{13}$$

l can be expressed as

$$l = \int_0^{l_0} \sqrt{1 + \left(\frac{\partial u}{\partial Y} \right)^2} dY \tag{14}$$

Then, δY have the form

$$\delta Y = l - l_0 = \int_0^{l_0} \sqrt{1 + \left(\frac{\partial u}{\partial Y} \right)^2} dY - l_0 = \int_0^{l_0} \left[\sqrt{1 + \left(\frac{\partial u}{\partial Y} \right)^2} - 1 \right] dY \tag{15}$$

Axis curve of the work roll microelement is expanded by Taylor series

$$\Delta Y \sqrt{1 + \left(\frac{\partial u}{\partial Y} \right)^2} = \Delta Y \left[1 + \frac{1}{2} \left(\frac{\partial u}{\partial Y} \right)^2 - \frac{1}{8} \left(\frac{\partial u}{\partial Y} \right)^4 + \dots \right] \tag{16}$$

Due to δY is very small, then $l \approx l_0$, and omit the items over the third power in Eq. (16), we have

$$\delta Y = \frac{1}{2} \int_0^{l_0} \left(\frac{\partial u}{\partial Y} \right)^2 dY \tag{17}$$

Substituting Eqs. (17) and (12) into (11) yields

$$m \frac{\partial^2 u}{\partial \bar{t}^2} + c \frac{\partial u}{\partial \bar{t}} + E_1 I \frac{\partial^4 u}{\partial Y^4} - \rho I \left(1 + \frac{E_1}{\kappa G} \right) \frac{\partial^4 u}{\partial Y^2 \partial \bar{t}^2} + \left[\frac{\mu P \sin \theta \cos \omega \bar{t}}{\cos \alpha} - \rho I \bar{\Omega}^2 - \frac{E_1 A}{2l} \int_0^l \left(\frac{\partial u}{\partial Y} \right)^2 dY \right] \frac{\partial^2 u}{\partial Y^2} = 0 \tag{18}$$

Let the roll's deflection u be a unimodal basis function

$$u = \bar{u}(\bar{t}) \left(1 - \cos \frac{2\pi}{l} Y \right) \tag{19}$$

Substitute Eqs. (19) into (18), Galerkin method make the weighted residual integral of the original control equation equal to zero to obtain the following control equation

$$\int_0^l \left(1 - \cos \frac{2\pi}{l} Y \right) \left[m \left(1 - \cos \frac{2\pi}{l} Y \right) \frac{\partial^2 \bar{u}}{\partial \bar{t}^2} + c \left(1 - \cos \frac{2\pi}{l} Y \right) \frac{\partial \bar{u}}{\partial \bar{t}} - \rho I \left(1 + \frac{E_1}{\kappa G} \right) \frac{\partial^2 \bar{u}}{\partial \bar{t}^2} \left(\frac{2\pi}{l} \right)^2 \cos \left(\frac{2\pi}{l} \right) Y - E_1 I \bar{u} \left(\frac{2\pi}{l} \right)^4 \cos \left(\frac{2\pi}{l} \right) Y + \left(\frac{\bar{u} \mu P \sin \theta \cos \omega \bar{t}}{\cos \alpha} - \bar{u} \rho I \bar{\Omega}^2 - \frac{E_1 A \bar{u}^3 \pi^2}{l^2} \right) \left(\frac{2\pi}{l} \right)^2 \cos \left(\frac{2\pi}{l} \right) Y \right] dY = 0 \tag{20}$$

Differential equation can be obtained through integration

$$\left[m + \rho I \left(1 + \frac{E_1}{\kappa G} \right) \left(\frac{2\pi}{l} \right)^2 \right] \ddot{\bar{u}} + c \dot{\bar{u}} + \left(\frac{2\pi}{l} \right)^2 \left[E_1 I \left(\frac{2\pi}{l} \right)^2 + \rho I \bar{\Omega}^2 - \frac{\mu P \sin \theta \cos \omega \bar{t}}{\cos \alpha} \right] \bar{u} + \frac{E_1 A \bar{u}^3 \pi^2}{l^2} \left(\frac{2\pi}{l} \right)^2 = 0 \tag{21}$$

Nondimensionalizing Eq. (21), let

$$x = \frac{\bar{u}}{l}, \Omega = \frac{\omega l^2}{2} \sqrt{\frac{\kappa m G l^2 + 4\pi^2 \rho I (E_1 + \kappa G)}{\kappa G l^2 E_1 I}}, t = \frac{\bar{t}}{l^2} \sqrt{\frac{\kappa G l^2 E_1 I}{\kappa m G l^2 + 4\pi^2 \rho I (E_1 + \kappa G)}} \tag{22}$$

$$c_1 = \frac{c l^3 \sqrt{\kappa G}}{\sqrt{E_1 I [\kappa m G l^2 + 4\pi^2 \rho I (E_1 + \kappa G)]}}, F_0 = \frac{\mu P l^2 \sin \theta}{E_1 I \cos \alpha}, \omega_0^2 = \frac{4\pi^2 \rho I \bar{\Omega}^2 l^2 + 16\pi^4 E_1 I}{E_1 I}$$

Therefore, the motion equation of work roll's horizontal vibration under the action of axial load excitation can be obtained as follows

$$\ddot{x} + c_1 \dot{x} + [\omega_0^2 + k_1 \cos(2\Omega t)] x + k_3 x^3 = 0 \tag{23}$$

where ω_0 denotes the work roll's inherent frequency³⁵, the parametric excitation stiffness ratio $k_1 = 4\pi^2 F_0$ is proportional to the dynamic rolling force amplitude, and $k_3 = 4\pi^4 A l^2 / I$ is the cubic stiffness ratio. In terms of the universality of Mathieu equation's solution, when the value of Ω/ω_0 takes different values, the corresponding physical system has an unstable state, therein the formation of system resonance would appear in many regions^{36,37} (Arnold resonance tongues). What's more, when $\Omega/\omega_0 = 1$, it corresponds to the maximum first-order Arnold resonance tongue on parameters plane of Mathieu equation. From the stability of the systematic whole workspace, under this working condition of $\Omega/\omega_0 = 1$, the systematic unstable region has the largest distribution range and the effective workspace is the smallest. Therefore, in order to optimize the systematic workspace to obtain greater effective space, it is necessary to explore the stability of the system in the workspace with the worst stability. To sum up, the following discussion focuses on the dynamic characteristics of the roll's horizontal vibration system as the frequency ratio Ω/ω_0 varies in the vicinity of $\Omega/\omega_0 = 1$. The flowchart for the specific modeling mentioned above can be found in Online Appendix Fig. 1.

Numerical results and discussion

Perturbation analysis

In this section, active damping and active stiffness bivariate time-delay control signals are introduced to the roll's horizontal vibration system (23) under axial load excitation, and the amplitude-frequency characteristics of the primary parameter resonance corresponding to the maximum Arnold resonance tongue are resolved by the multi-scale method to analyze the steady-state response of the system in the workspace with the worst stability.

Introducing active control signal, the control equation for the systematic horizontal vibration under axial load can be obtained as follows

$$\ddot{x} + c_1\dot{x} + [\omega_0^2 + k_1 \cos(2\Omega t)]x + k_3x^3 = g_1x(t - t_d) + g_2\dot{x}(t - t_d) \tag{24}$$

where g_1 is the displacement gain, g_2 is the velocity gain, and t_d represents the time delay.

According to the theory of multi-scale method, a small parameter η is introduced, let $c_1 = \eta c_1$, $k_1 = \eta k_1$, $k_3 = \eta k_3$, $g_1 = \eta g_1$, $g_2 = \eta g_2$, $\Omega = \omega_0 + \eta\sigma$, where σ is the frequency tuning parameter.

Thus, the Eq. (24) can be written as

$$\ddot{x} + \omega_0^2x = -\eta c_1\dot{x} - \eta k_3x^3 - \eta k_1 \cos(2\Omega t)x + \eta g_1x(t - t_d) + \eta g_2\dot{x}(t - t_d) \tag{25}$$

Assuming Eq. (25) has the following form of solution

$$\begin{cases} x(t, \eta) = x_0(T_0, T_1) + \eta x_1(T_0, T_1) \\ x_\tau(t, \eta) = x_{0\tau}(T_0, T_1) + \eta x_{1\tau}(T_0, T_1) \end{cases} \tag{26}$$

where $x_0(T_0, T_1)$ and $x_{0\tau}(T_0, T_1)$ respectively represent the perturbation solution and its time delayed perturbation solution. T_0 and T_1 denote the fast and slow time scales.

Taking the derivative of the time scale yields the differential operator as

$$\begin{cases} \frac{d}{dt} = \frac{\partial}{\partial T_0} + \eta \frac{\partial}{\partial T_1} + \dots = D_0 + \eta D_1 + \dots \\ \frac{d^2}{dt^2} = (D_0 + \eta D_1 + \dots)^2 = D_0^2 + 2\eta D_0 D_1 + \dots \end{cases} \tag{27}$$

where $D_m n = \partial^m / \partial T_n^m$ represents the m -th order partial derivative with respect to the n -th time scale.

Substitute Eqs. (26) into (25) and expand it, so that the coefficients of η^0 and η^1 on both sides of the equation are equal. After sorting, we can obtain

$$D_0^2x_0 + \omega_0^2x_0 = 0 \tag{28}$$

$$D_0^2x_1 + \omega_0^2x_1 = -2D_0D_1x_0 - c_1D_0x_0 - k_1 \cos(2\Omega T_0)x_0 - k_3x_0^3 + g_1x_{0\tau} + g_2D_0x_{0\tau} \tag{29}$$

Let the form of the solution to Eq. (28) be

$$\begin{cases} x_0(T_0, T_1) = A(T_1)e^{j\omega_0T_0} + cc \\ x_{0\tau}(T_0, T_1) = A_1(T_1)e^{j\omega_0T_0 - j\tau} + cc \end{cases} \tag{30}$$

where cc is the conjugate term, which is not described below, and $\tau = \Omega t_d$.

Substituting Eqs. (30) into (29) and combining similar e-exponential functions yields

$$D_0^2x_1 + \omega_0^2x_1 = ST_1e^{j\omega_0T_0} - \left(\frac{1}{2}k_1A + k_3A^3\right)e^{3j\omega_0T_0} + cc \tag{31}$$

where ST_1 is the duration term, which is expressed as

$$ST_1 = -2j\omega_0D_1A - j\omega_0c_1A - \frac{1}{2}k_1\bar{A}e^{2j\sigma T_1} - 3k_3A^2\bar{A} + (g_1 + j\omega_0g_2)Ae^{-j\tau} \tag{32}$$

Let the special solution A of the complex amplitude be expressed in polar coordinates as follows

$$A = \frac{1}{2}ae^{j\psi} \tag{33}$$

where a and ψ are real functions of T_1 .

Substituting Eqs. (33) into (32) and making the duration term equal to zero yields

$$-j\omega_0D_1a + a\omega_0D_1\psi - \frac{1}{2}j\omega_0c_1a - \frac{1}{4}k_1ae^{2j(\sigma T_1 - \psi)} - \frac{3}{8}k_3a^3 + \frac{1}{2}(g_1 + j\omega_0g_2)ae^{-j\tau} = 0 \tag{34}$$

Let $\varphi = \sigma T_1 - \psi$, separating the real and imaginary parts gives

$$\frac{da}{dT_1} = \frac{1}{\omega_0} \left(-\frac{1}{2}\omega_0c_1a - \frac{1}{4}k_1a \sin 2\varphi - \frac{1}{2}g_1a \sin \tau + \frac{1}{2}\omega_0g_2a \cos \tau \right) \tag{35}$$

$$\frac{d\varphi}{dT_1} = \sigma - \frac{1}{a\omega_0} \left(\frac{1}{4}k_1a \cos 2\varphi + \frac{3}{8}k_3a^3 - \frac{1}{2}g_1a \cos \tau - \frac{1}{2}\omega_0g_2a \sin \tau \right) \tag{36}$$

When the system has no control pattern, i.e., active control parameters $g_1 = 0$, $g_2 = 0$ and $\tau = 0$, by solving Eqs. (35) and (36), the steady-state response of the systematic parameter resonance can be obtained as shown in Fig. 5.

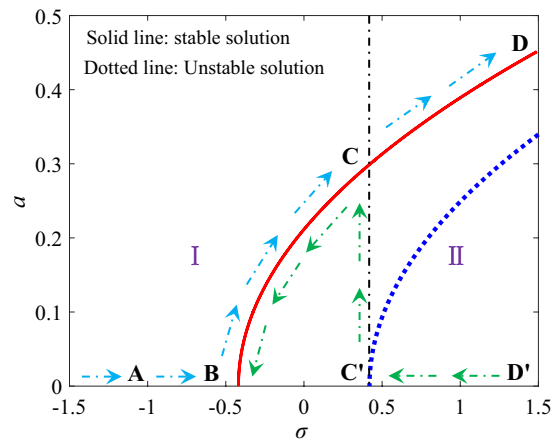


Fig. 5. Steady state response curve of parameter resonance.

The steady-state response curve depicted in Fig. 5 demonstrates the typical hardening-type hysteresis characteristics of roll's horizontal vibration under the resonance condition $\Omega/\omega_0 = 1$. The solid line represents stable nontrivial solutions, while the dashed line represents unstable nontrivial solutions. When the excitation parameter is much lower than twice the system frequency (point A in region I), the system exhibits only one stable nontrivial solution, demonstrating low-amplitude resonance under this condition. As the tuning parameter σ increases to point B, the system undergoes a saddle-node bifurcation and the resonance amplitude rapidly increases. As the excitation frequency approaches twice the system frequency, i.e. $\sigma = 0$, the amplitude of stable nontrivial responses rapidly increases until an unstable non trivial solution appears at point C, at which point the system transitions to the unstable region II. On the other hand, as the excitation frequency decreases from the point D', the systematic response amplitude a exhibits low-amplitude resonance along the D'-C' path and when the tuning parameter reaches another saddle-node bifurcation point C', the amplitude a undergoes a jump phenomenon and increases rapidly to the coexisting stable nontrivial solution (point C). Subsequently, the amplitude decreases by further reducing the tuning parameter until point A. As observed, under resonance conditions, the systematic horizontal vibration undergoes two catastrophic bifurcations (points B and C'). When the tuning parameters are increased and decreased, the frequency response curves follow paths of ABCD and D'C'CB A, respectively, and the system may exhibit different resonance behaviors. This hysteresis phenomenon under primary resonance conditions arises due to the presence of multiple coexisting nontrivial solutions. Furthermore, from Fig. 5, it is evident that within the range $\sigma_C < \sigma < \sigma_D$ (region II), there exists a stable nontrivial solution and an unstable nontrivial solution for resonance amplitude, and the systematic response in this region varies with different initial conditions of the system.

To verify and optimize the theoretical model under actual working conditions, an experimental platform was built for frequency sweep testing to verify the predicted resonance behavior and improve the engineering relevance of the model.

Based on the above theoretical analysis, the roll system experiences an additional axial force due to the gyroscopic effect. According to the force characteristics during the rolls' working process in a four-roll cold rolling mill, an identical mechanical system arrangement is applied to the work roll on the experimental platform shown in Fig. 6. The experiment used an accelerometer installed on the outer side of the frame corresponding to the work roll bearing seat to measure the horizontal vibration signal.

During the experiment, an excitation loading device was used to apply axial excitation to the end of the work roll's journal to simulate the axial force. Frequency sweep experiments were conducted under different excitation amplitudes to measure the time-domain signal of the roll's horizontal vibration acceleration. The excitation amplitude was determined by the power amplifier of the loading system, and the excitation frequency was adjusted by a function generator.

Before the formal testing, the rolling mill was allowed to run for a period to reach a stable vibration state. Modal testing was conducted using the hammering method to obtain the free vibration response of the work roll, as shown in Fig. 7. Spectral analysis confirms that the first-order system frequency of the roll is 33.4 Hz, and the 2nd, 3rd and 4th order system frequencies are 79.4 Hz, 103.9 Hz and 153.8 Hz, respectively.

Since the maximum resonant tongue occurs near the axial load excitation frequency twice the roll's systematic frequency. Therefore, during the experiment, a sweep frequency experiment is conducted near twice the first-order system frequency (i.e., 66.8 Hz), aiming to experimentally verify the systematic 1st order Arnold resonance tongue region. During the experiment, adjust the power amplifier to set the axial excitation voltage to five values: 3.8 V, 3 V, 2.2 V, 1.8 V, and 1.4 V. For each different load value, the function generator was manually adjusted to vary the excitation frequency in steps of 2 Hz/s within the 40–100 Hz range. At the same time, use a data acquisition module to record the experimental data. By observing the time-domain signal and determining the upper and lower limits of the corresponding critical frequency based on the changes in vibration frequency per unit time, the test results of the first-order dynamic instability domain under different axial load excitations can be obtained as shown in Fig. 8.

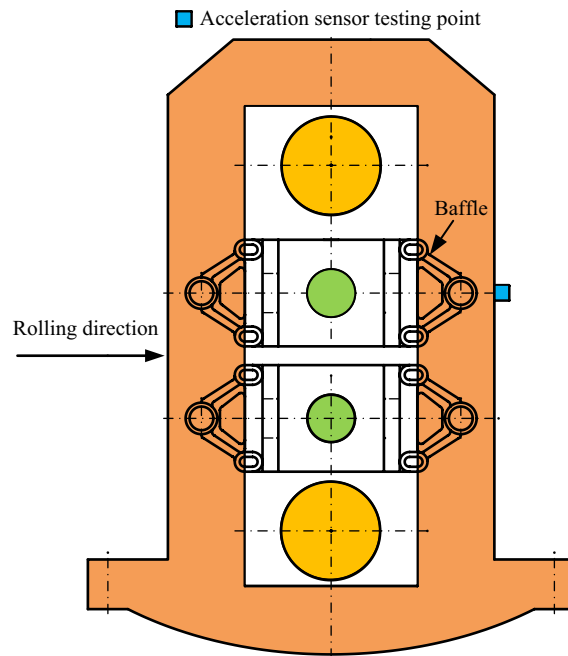


Fig. 6. Four-high mill experimental platform.

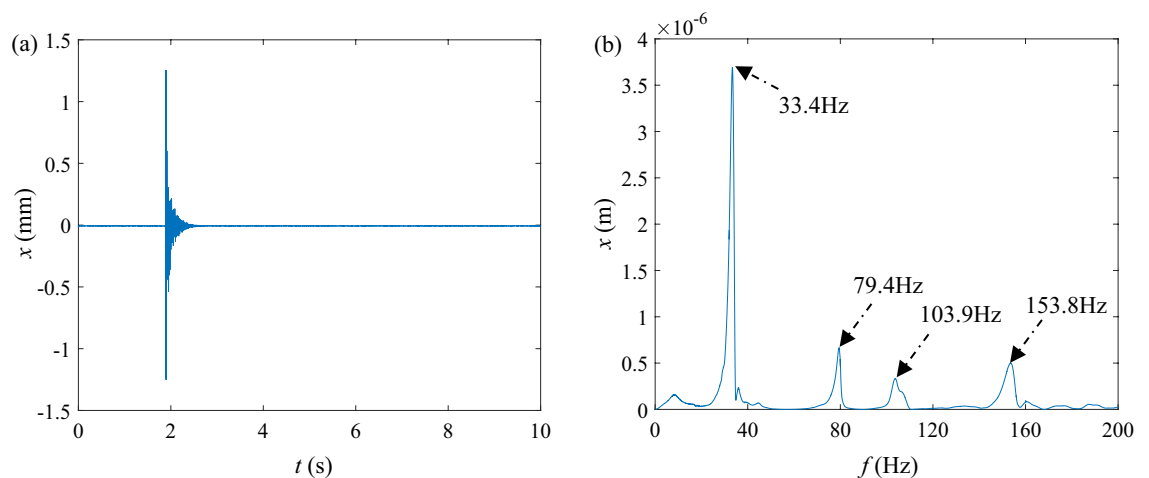


Fig. 7. Time domain and frequency spectrum analysis of hammering test, (a) time domain signal (b) frequency domain signal.

During the sweep frequency process, resonance was identified when the amplitude continuously exceeded 0.5 mm. Based on the known sweep rate, the time-domain signal in Fig. 8 was converted to the corresponding excitation frequency. (i.e., approximately twice the systematic natural frequency). The calculated excitation frequency values and the corresponding vibration amplitudes were then plotted in Fig. 5, resulting in a comparison between the theoretical and experimental results of the nonlinear steady-state vibration response, as shown in Fig. 9.

As shown in Fig. 9, the nonlinear steady-state vibration response curve (as shown in Fig. 5) obtained from theoretical analysis generally agrees with the overall trend of the experimental data points. However, in the non-resonant regions, the experimentally measured amplitudes are generally larger than those predicted by the steady-state response. This discrepancy may be attributed to random excitations present in the experimental environment. The nonlinear response curve exhibits a distinct rightward bending toward higher excitation frequencies, indicating a typical hardening spring behavior. This suggests that the horizontal vibration of the work roll during rotation tends to shift toward higher frequencies, displaying a traction-like response.

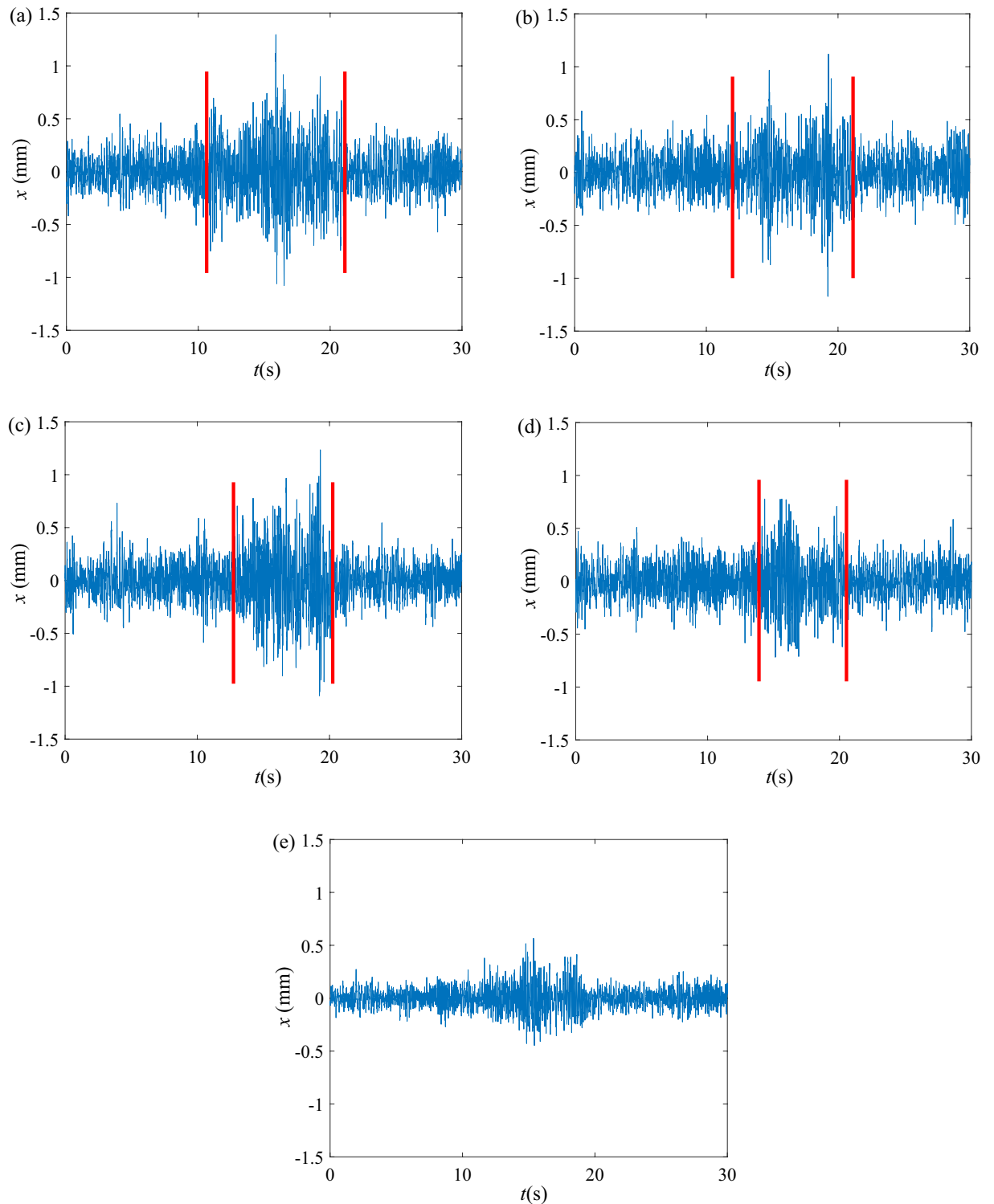


Fig. 8. Time domain diagram of acceleration signal under sweeping frequency excited by different axial loads, (a) 3.8V (b) 3V (c) 2.2V (d) 1.8V (e) 1.4V.

Bifurcation and chaos analysis

To investigate the nonlinear dynamic bifurcation and chaotic characteristics in the unstable state space associated with resonance-induced instability, bifurcation theory and Lyapunov exponents are employed to quantitatively describe the evolution of the system's dynamic behavior under the condition of $\Omega/\omega_0 = 1$.

Taking a 1850 four-high cold rolling mill as an example, the following working parameters are used for simulation: horizontal equivalent damping $4.86 \times 10^5 \text{ N}\cdot\text{s/m}$, equivalent parametric excitation stiffness

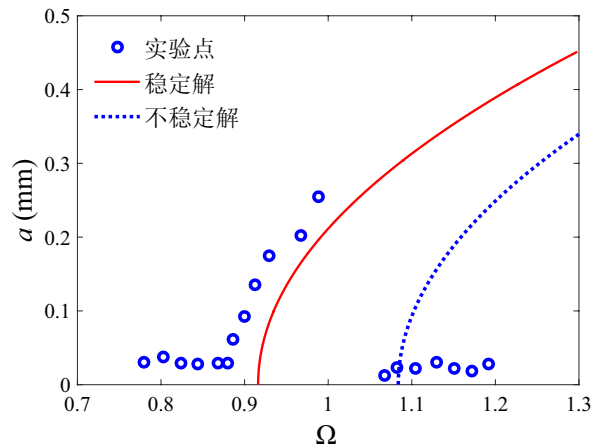


Fig. 9. Comparison of theoretical and experimental results of steady state response.

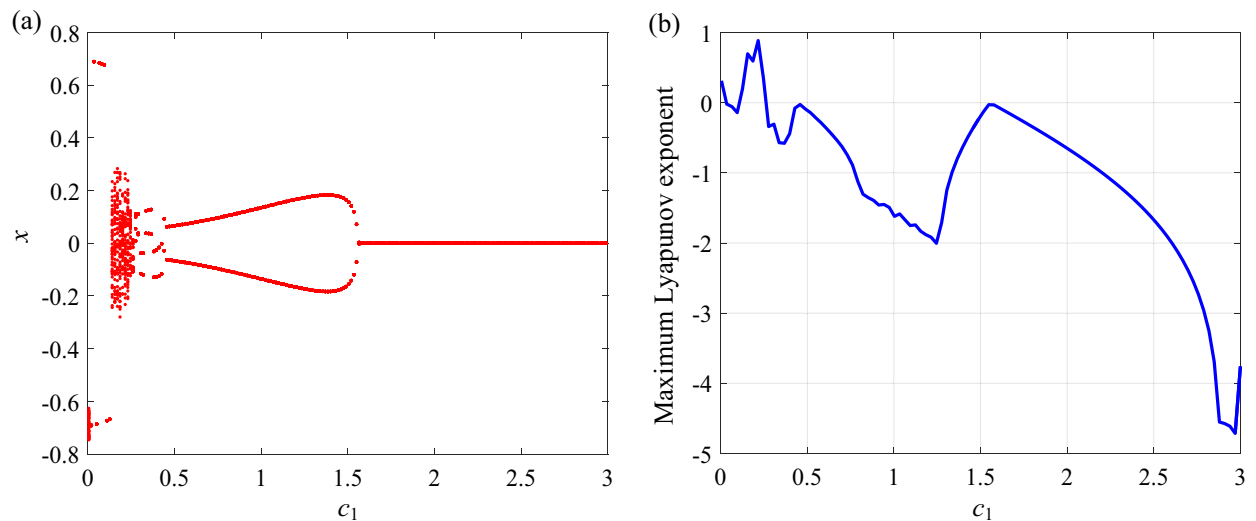


Fig. 10. Bifurcation and maximum Lyapunov exponent graph with c_1 variation.

coefficient $1.41 \times 10^6 \text{ N/m}$, and equivalent cubic stiffness $1.96 \times 10^7 \text{ N/m}^3$. According to Eqs. (2–24), the corresponding dimensionless parameters are calculated as $c_1 = 0.173$, $\Omega = 1$, $k_1 = 1.8$, $k_3 = 25$. The Runge–Kutta method is employed to numerically solve Eq. (3–1), and the bifurcation characteristics as well as the patterns of the maximum Lyapunov exponent under different structural parameter conditions are obtained, as shown in Figs. 10, 11 and 12.

As shown in Fig. 10, increasing the damping ratio c_1 leads to a dynamic transition from chaotic motion to quasi-periodic, then to period-doubling, and finally to single-periodic behavior. When $c_1 \in [0, 0.25]$, Fig. 10b indicates that the maximum Lyapunov exponent is greater than zero, suggesting that the system exhibits chaotic behavior and unstable vibration. At $c_1 = 0.25$, the system transitions from chaos to multi-periodic motion, with the maximum Lyapunov exponent becoming negative. When $c_1 = 0.47$, the system further transitions to a period-2 motion, and for $c_1 > 1.565$, the system enters a stable periodic orbit. These results indicate that as c_1 increases, the system ultimately tends toward a stable single-periodic motion, confirming that increasing the damping coefficient contributes to improved stability of the system's dynamic response.

From Fig. 11, the system remains in a single-periodic motion state when $k_1 = 0–0.342$. At $k_1 = 0.342$, a period-doubling bifurcation occurs, and the system transitions from single-periodic to period-2 motion. In this range, the corresponding maximum Lyapunov exponents remain negative, indicating stable behavior. However, when $k_1 = 3.3$, the system undergoes a sudden destabilization, and chaotic behavior emerges within the range $k_1 \in [3.3, 3.6]$, indicating an unstable dynamic state. These results demonstrate that as the parametric stiffness ratio k_1 increases, the system transitions from a stable periodic state to an unstable chaotic regime, thereby weakening the overall dynamic stability.

From Fig. 12, the system exhibits chaotic behavior when $k_3 = 0–0.912$. In the range $k_3 = 0.912–4.674$, the system enters a single-periodic motion state. When $k_3 > 4.674$, the system transitions back from periodic to

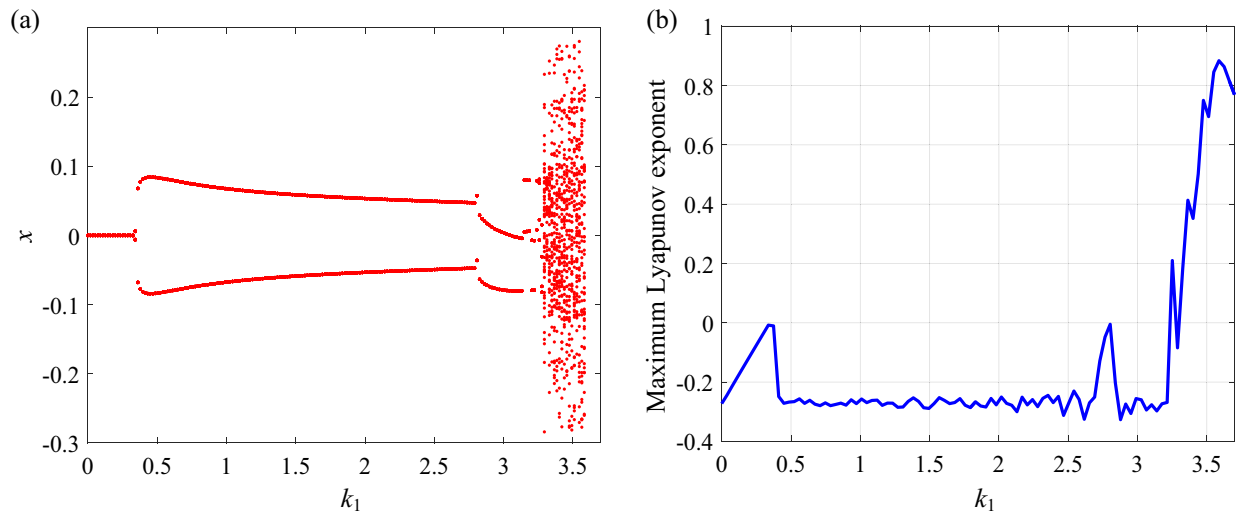


Fig. 11. Bifurcation and maximum Lyapunov exponent graph with k_1 variation.

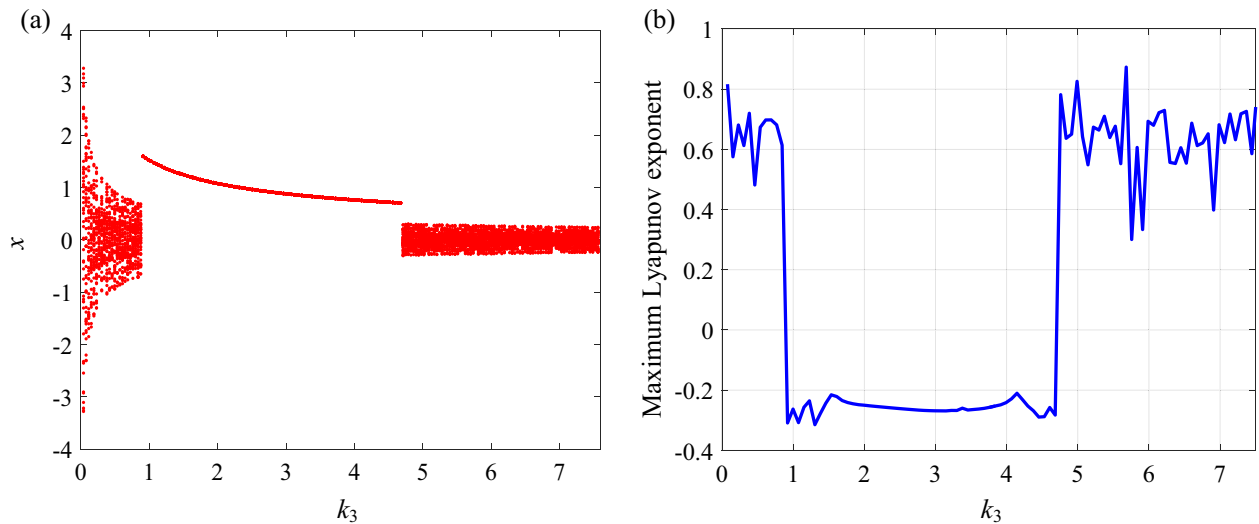


Fig. 12. Bifurcation and maximum Lyapunov exponent graph with k_3 variation.

chaotic motion, as indicated by a positive maximum Lyapunov exponent. These results suggest that when the cubic stiffness ratio k_3 is small, the system exhibits weak nonlinearity, low sensitivity to operating condition variations, and relatively good stability. However, as k_3 increases, the degree of nonlinearity in the system becomes more pronounced, leading to heightened sensitivity to small disturbances and a higher likelihood of chaotic motion, thereby increasing the system's instability.

Mode energy orbit evolution characteristics of nonlinear horizontal vibration on rolls

In addition to the method of multiple scales, the Homotopy Analysis Method is employed in this study due to its flexibility in handling strong nonlinearities and its ability to control convergence via the auxiliary parameter h , making it a valuable complement to perturbation-based techniques. Until now, the focus and difficulty of using nonlinear theory to study nonlinear vibration problems is how to construct an approximate analytical method that does not depend on small parameters and has good convergence properties. Due to the limitations of traditional nonlinear methods, Liao³⁸ introduced the concept of homotopy into differential equations from a mathematical point of view, and proposed a new method for solving the mechanical problems of strongly nonlinear systems, i.e., homotopy analysis method. In recent years, the advantages of homotopy analysis in analytical approaches have become increasingly apparent, and it has successfully addressed strongly nonlinear vibration problems in various engineering fields. Through simulation, unique and interesting nonlinear phenomena have been discovered, which profoundly reveals the nonlinear characteristics of different engineering systems.

To compare and analyze the steady-state response curves of parametric resonance corresponding to the maximum Arnold resonance tongue shown in Fig. 5 of section “Perturbation analysis” and to find out the more complicated and interesting nonlinear phenomena, homotopy method is further applied to analyze the dynamic response of nonlinear horizontal vibration in a four-roll cold-rolling system, and to study nonlinear characteristics of multi-order modal energy orbit evolution.

In this study, the homotopy operator is constructed based on the original nonlinear equation of motion by defining a linear operator chosen to satisfy linearity and the boundary conditions. The homotopy deformation equation is then formulated to continuously deform the initial guess solution into the actual solution of the nonlinear system, under the control of the convergence parameter.

Firstly, the characteristic polynomial of the auxiliary differential operator is established as

$$P(\lambda) = \lambda \prod_{r=1}^3 (\lambda + r\Omega i) (\lambda - r\Omega i) \tag{37}$$

According to Eq. (37), the auxiliary operator is constructed as follows

$$\ell_4(x) = x^{(7)} + 14\Omega^2 x^{(5)} + 49\Omega^4 x^{(3)} + 36\Omega^6 \dot{x} \tag{38}$$

For Eq. (23), the homotopy operator is constructed as

$$\wp(x, q) = \ell_4(x) - q \left\{ \ell_4(x) + \hbar H(t) \left\{ \ddot{x} + c_1 \dot{x} + [\omega_0^2 + k_1 \cos(2\Omega t)] x + k_3 x^3 \right\} \right\} \tag{39}$$

where $q \in [0, 1]$ is an embedding parameter, \hbar is a nonzero auxiliary parameter, and $H(t)$ is the auxiliary function.

Assume that the solution of Eq. (23) can be expressed as

$$x = x_0 + qx_1 + q^2 x_2 + \dots \tag{40}$$

Substitute Eqs. (40) into (39), merge the same power terms of q , and give the same power order of q , thereby obtaining the following expression

$$q^0 : \ell_4(x_0) = 0 \tag{41}$$

$$q^1 : \ell_4(x_1) = \ell_4(x_0) + \hbar H(t) \left\{ \ddot{x}_0 + c_1 \dot{x}_0 + [\omega_0^2 + k_1 \cos(2\Omega t)] x_0 + k_3 x_0^3 \right\} = 0 \tag{42}$$

The solution to Eq. (41) can be approximated by the 4th-order frequency

$$x_0 = A_0 + \sum_{r=1}^3 [B_r \cos(r\Omega t) + C_r \sin(r\Omega t)] \tag{43}$$

where A_0, B_0, C_0 and D_0 are coefficients to be determined.

Substituting Eqs. (43) and (41) into (42), we obtain

$$\begin{aligned} \ell_4(x_1) = & -\hbar H(t) \left\{ \sum_{r=1}^3 [(r\Omega)^2 B_r \cos(r\Omega t) + (r\Omega)^2 C_r \sin(r\Omega t)] - c_1 \sum_{r=1}^3 [r\Omega B_r \right. \\ & \left. \cos(r\Omega t) + r\Omega C_r \sin(r\Omega t)] - \omega_0^2 A_0 - \omega_0^2 \sum_{r=1}^3 [B_r \cos(r\Omega t) + C_r \sin(r\Omega t)] \right. \\ & \left. - k_1 A_0 \cos(\Omega t) - \frac{k_1}{2} \sum_{r=1}^3 \{ B_r [\cos(r+1)\Omega t + \cos(r-1)\Omega t] \right. \\ & \left. + C_r [\sin(r+1)\Omega t + \sin(r-1)\Omega t] \} - k_3 \Theta \right\} \end{aligned} \tag{44}$$

where

$$\begin{aligned} \Theta = & A_0^3 + 3A_0^2 \sum_{r=1}^3 [B_r \cos(r\Omega t) + C_r \sin(r\Omega t)] + \frac{3}{2} A_0 \sum_{r=1}^3 \sum_{s=1}^3 B_r B_s [\cos(r+s)\Omega t \\ & + \cos(r-s)\Omega t] + 3A_0 \sum_{r=1}^3 \sum_{s=1}^3 B_r C_s [\sin(r+s)\Omega t - \sin(r-s)\Omega t] - \frac{3}{2} A_0 \sum_{r=1}^3 \sum_{s=1}^3 C_r C_s \\ & [\cos(r+s)\Omega t - \cos(r-s)\Omega t] \end{aligned}$$

$$\begin{aligned}
 & + \frac{1}{4} \sum_{m=1}^3 \sum_{r=1}^3 \sum_{s=1}^3 B_m B_r B_s [\cos(m+r+s)\Omega t \\
 & + \cos(m-r-s)\Omega t + \cos(m+r-s)\Omega t + \cos(m-r+s)\Omega t] + \frac{1}{2} \sum_{m=1}^3 \sum_{r=1}^3 \sum_{s=1}^3 B_m B_r C_s \\
 & [\sin(m+r+s)\Omega t - \sin(m-r-s)\Omega t - \sin(m+r-s)\Omega t + \sin(m-r+s)\Omega t] \\
 & - \frac{1}{4} \sum_{m=1}^3 \sum_{r=1}^3 \sum_{s=1}^3 B_m C_r C_s [\cos(m+r+s)\Omega t + \cos(m-r-s)\Omega t - \cos(m+r-s)\Omega t \\
 & - \cos(m-r+s)\Omega t] + \frac{1}{4} \sum_{m=1}^3 \sum_{r=1}^3 \sum_{s=1}^3 C_m B_r B_s [\sin(m+r+s)\Omega t + \sin(m-r-s)\Omega t \\
 & + \sin(m+r-s)\Omega t + \sin(m-r+s)\Omega t] - \frac{1}{2} \sum_{m=1}^3 \sum_{r=1}^3 \sum_{s=1}^3 C_m B_r C_s [\cos(m+r+s)\Omega t \\
 & - \cos(m-r-s)\Omega t - \cos(m+r-s)\Omega t + \cos(m-r+s)\Omega t] - \frac{1}{4} \sum_{m=1}^3 \sum_{r=1}^3 \sum_{s=1}^3 C_m C_r C_s \\
 & [\sin(m+r+s)\Omega t + \sin(m-r-s)\Omega t - \sin(m+r-s)\Omega t - \sin(m-r+s)\Omega t]
 \end{aligned}$$

From Eq. (44), seven algebraic equations f_i ($i=1,2,\dots,7$) are constructed, corresponding to the seven secular terms of $x_1(t)$. To eliminate the secular terms, let $f_i=0$ ($i=1,2,\dots,7$), which is calculated as follows

$$\begin{aligned}
 0^{\text{th}} \text{ - order : } f_1 = & \omega_0^2 A_0 + k_3 A_0^3 + \frac{3}{2} k_3 A_0 (B_1^2 + B_2^2 + B_3^2) + \frac{3}{2} k_3 A_0 (C_1^2 + C_2^2 + C_3^2) + \frac{3}{4} k_3 B_1^2 B_2 + \\
 & \frac{3}{2} k_3 B_1 B_2 B_3 - \frac{3}{4} k_3 B_2 C_1^2 - \frac{3}{2} k_3 B_3 C_1 C_2 + \frac{3}{2} k_3 B_2 C_1 C_3 + \frac{3}{2} k_3 B_1 C_2 (C_3 + C_1) = 0
 \end{aligned} \tag{45}$$

$$\begin{aligned}
 \cos \Omega t : f_2 = & -\Omega^2 B_1 + c_1 \Omega B_1 + \omega_0^2 B_1 + k_1 A_0 \\
 & + \frac{1}{2} k_1 B_2 + 3k_3 A_0^2 B_1 + 3k_3 A_0 B_1 B_2 + 3k_3 A_0 B_2 B_3 \\
 & + 3k_3 A_0 C_1 C_2 + 3k_3 A_0 C_2 C_3 \\
 & + \frac{3}{4} k_3 (B_1^3 + B_1^2 B_3 + 2B_1 B_3^2 + B_2^2 B_3 + 2B_1 B_2^2) \\
 & + \frac{3}{4} k_3 (B_1 C_1^2 - B_3 C_1^2 + 2B_1 C_1 C_3 + 2B_2 C_2 C_3 + 2B_1 C_2^2 - B_3 C_2^2 + 2B_1 C_3^2) = 0
 \end{aligned} \tag{46}$$

$$\begin{aligned}
 \sin \Omega t : f_3 = & -\Omega^2 C_1 + c_1 \Omega C_1 + \omega_0^2 C_1 + \frac{1}{2} k_1 C_2 + 3k_3 A_0^2 C_1 + 3k_3 A_0 B_1 C_2 - 3k_3 A_0 B_2 C_1 \\
 & + 3k_3 A_0 B_2 C_3 - 3k_3 A_0 B_3 C_2 + \frac{3}{4} k_3 (C_1^3 - C_1^2 C_3 + 2C_1 C_2^2 + C_2^2 C_3 + 2C_1 C_3^2) \\
 & + \frac{3}{4} k_3 (B_1^2 C_1 + B_1^2 C_3 + 2B_2^2 C_1 - B_2^2 C_3 + 2B_3^2 C_1 - 2B_1 B_3 C_1 + 2B_2 B_3 C_2) = 0
 \end{aligned} \tag{47}$$

$$\begin{aligned}
 \cos 2\Omega t : f_4 = & -4\Omega^2 B_2 + 2c_1 \Omega B_2 + \omega_0^2 B_2 + \frac{1}{2} k_1 (B_1 + B_3) + 3k_3 A_0^2 B_2 + \frac{3}{2} k_3 A_0 B_1 (B_1 + 2B_3) \\
 & - \frac{3}{2} k_3 A_0 C_1^2 + 3k_3 A_0 C_1 C_3 + \frac{3}{4} k_3 (B_2^3 + 2B_1^2 B_2 + 2B_2 B_3^2 + 2B_1 B_2 B_3) \\
 & + \frac{3}{4} k_3 (2B_2 C_1^2 + 2B_3 C_1 C_2 - 2B_2 C_1 C_3 + 2B_1 C_2 C_3 + B_2 C_2^2 + 2B_2 C_3^2) = 0
 \end{aligned} \tag{48}$$

$$\begin{aligned}
 \sin 2\Omega t : f_5 = & -4\Omega^2 C_2 + 2c_1 \Omega C_2 + \omega_0^2 C_2 + \frac{1}{2} k_1 (C_1 + C_3) + 3k_3 A_0^2 C_2 + 3k_3 A_0 B_1 (C_1 + C_3) \\
 & - 3k_3 A_0 B_3 C_1 + \frac{3}{4} k_3 (C_2^3 + 2C_1^2 C_2 + 2C_2 C_3^2 + 2C_1 C_2 C_3) \\
 & + \frac{3}{4} k_3 (2B_1^2 C_2 + B_2^2 C_2 + 2B_3^2 C_2 + 2B_1 B_2 B_3 - 2B_1 B_3 C_2 + 2B_2 B_3 C_1) = 0
 \end{aligned} \tag{49}$$

$$\begin{aligned}
 \cos 3\Omega t : f_6 = & -9\Omega^2 B_3 + 3c_1 \Omega B_3 + \omega_0^2 B_3 + \frac{1}{2} k_1 B_2 + 3k_3 A_0^2 B_3 + 3k_3 A_0 B_1 B_2 \\
 & - 3k_3 A_0 C_1 C_2 + \frac{1}{4} k_3 (B_1^3 + 6B_1^2 B_3 + 6B_2^2 B_3 + 3B_3^3 + 3B_1 B_2^2) \\
 & - \frac{3}{4} k_3 (B_1 C_1^2 - 2B_3 C_1^2 - 2B_2 C_1 C_2 + B_1 C_2^2 - 2B_3 C_2^2 - B_3 C_3^2) = 0
 \end{aligned} \tag{50}$$

$$\begin{aligned} \sin 3\Omega t : f_7 = & -9\Omega^2 C_3 + 3c_1\Omega C_3 + \omega_0^2 C_3 + \frac{1}{2}k_1 C_2 + 3k_3 A_0^2 C_3 + 3k_3 A_0 B_1 C_2 \\ & + 3k_3 A_0 B_2 C_1 - \frac{1}{4}k_3 (C_1^3 - 6C_1^2 C_3 - 6C_2^2 C_3 - 3C_3^3 - 3C_1 C_2^2) \\ & + \frac{3}{4}k_3 (B_1^2 C_1 + 2B_1^2 C_3 - B_2^2 C_1 + 2B_2^2 C_3 + B_3^2 C_3 + 2B_1 B_2 C_2) = 0 \end{aligned} \quad (51)$$

The multivariate nonlinear equations represented by Eqs. (45)–(51) is equivalent to $F[(A,B,C)]=0$, and the corresponding Jacobi matrix $J[(A,B,C)]$ takes the form

$$J[(A,B,C)] = \begin{bmatrix} \frac{\partial f_1}{\partial A_0} & \frac{\partial f_1}{\partial B_1} & \frac{\partial f_1}{\partial C_1} & \frac{\partial f_1}{\partial B_2} & \frac{\partial f_1}{\partial C_2} & \frac{\partial f_1}{\partial B_3} & \frac{\partial f_1}{\partial C_3} \\ \frac{\partial f_2}{\partial A_0} & \frac{\partial f_2}{\partial B_1} & \frac{\partial f_2}{\partial C_1} & \frac{\partial f_2}{\partial B_2} & \frac{\partial f_2}{\partial C_2} & \frac{\partial f_2}{\partial B_3} & \frac{\partial f_2}{\partial C_3} \\ \vdots & \vdots & \vdots & \vdots & \vdots & \vdots & \vdots \\ \frac{\partial f_7}{\partial A_0} & \frac{\partial f_7}{\partial B_1} & \frac{\partial f_7}{\partial C_1} & \frac{\partial f_7}{\partial B_2} & \frac{\partial f_7}{\partial C_2} & \frac{\partial f_7}{\partial B_3} & \frac{\partial f_7}{\partial C_3} \end{bmatrix} \quad (52)$$

where, the terms of the Jacobian matrix (52) are provided in the Online Appendix Table 1.

Based on the Newton–Raphson iterative method, the iterative algorithm is obtained as follows

$$(A, B, C)^{k+1} = (A, B, C)^k - \{J[(A, B, C)^k]\}^{-1} \cdot F[(A, B, C)^k] \quad (53)$$

Substituting Eqs. (45)–(52) into the iterative algorithm (53), the values of A_0 , B_r and C_r ($r=1,2,3$) can be solved. The definitions of harmonic amplitude and phase are given by

$$A_r = \sqrt{B_r^2 + C_r^2}, \quad \varphi_r = \arctg(C_r/B_r) \quad (54)$$

The calculation flowchart of the Homotopy Analysis Method can be found in Online Appendix Fig. 2. According to Eqs. (53) and (54), the energy orbit evolution curves of the first 4th-order harmonic terms for the roll's horizontal vibration under the primary parametric resonance can be obtained, as shown in Fig. 13.

The first-order modal amplitude response shown in Fig. 13a represents steady-state response, while the higher-order modal amplitude responses shown in Fig. 13b–d exhibit fluctuating amplitudes. Figure 13a shows the energy orbit evolution curve of the first-order mode in the roll's horizontal vibration system corresponding to the maximum Arnold resonance tongue. From the figure, it is observed that the first-mode resonates when $\Omega/\omega_0 = 0.54$ – 2.153 , and the amplitude exhibits a jumping phenomenon. With the increase of the ratio of the excitation frequency to the system frequency, the response amplitude is also increased firstly and then decreased. Meanwhile, it can be seen that multiple frequency-locked regions appear when the amplitude jumps. Different platforms represent different locked frequencies, and the width of the platforms represents the size of the frequency-locked range. The change of frequency ratio on each platform does not change the modal amplitude. Figure 13b,c respectively depict the energy orbit evolution curve of the second and third modes with respect to the frequency ratio. From the figures, it can be observed that at $\Omega/\omega_0 = 0.54$, both the amplitudes of second-mode and third-mode undergo a bifurcation and sudden change. Then, the response amplitude starts to decrease with the reduction of the frequency ratio, and similarly multiple frequency-locked regions appear in the process of amplitude reduction, which exhibits an obvious nonlinear characteristic. Figure 13d shows the energy orbit evolution curve of the fourth-mode with respect to the frequency ratio. From the figure, it is evident that the fourth-mode amplitude increases with the increase of frequency ratio Ω/ω_0 , and multiple frequency-locked regions with unequal widths appear in the interval of Ω/ω_0 . As the frequency ratio increases, the frequency-locked regions have a self-similar structure with a devil's staircase morphology. Based on the analysis in the above figures, as the locking region transitions, bifurcations and abrupt amplitude jumps occur, which reveals the mutation mechanism driving sudden changes in the horizontal vibration of the rolling system as the frequency ratio varies. The “devil's staircase” represents a sequence of frequency-locked plateaus within the response space. Operationally, this means the system exhibits the same dynamic behavior within each staircase, but sudden bifurcations or amplitude jumps occur when transitioning between them. This insight helps guide practitioners to maintain the operating frequency ratio within a specific locking region, thereby avoiding abrupt changes in vibration levels.

By comparison, it is found that the overall change trends of the steady-state response curves of the primary parametric resonance solved by the multi-scale method in Fig. 5 and the first-order modal energy orbit evolution curves solved by the homotopy analysis method in Fig. 13a are consistent with each other, which both show that the amplitude firstly increases and then decreases with the increase of the frequency ratio, indicating the correctness of the homotopy analysis. In addition, it can be observed from Fig. 13 that as the frequency ratio changes, there are multiple frequency-locked regions in the system response, and a devil's staircase with chaotic characteristics is discovered, which further reveals the complex and interesting nonlinear characteristics of the system. This is because the homotopy analysis method has discovered some new solutions due to its unique solving advantages, which have been overlooked by multi-scale methods.

Energy evolution of the attractor of nonlinear horizontal vibration on rolls

Section “Mode energy orbit evolution characteristics of nonlinear horizontal vibration on rolls” reveals the energy orbit evolution characteristics under parameter resonance corresponding to the maximum Arnold resonance tongue of the roll's horizontal vibration system. Similarly, the manifold change of the attractor characterized

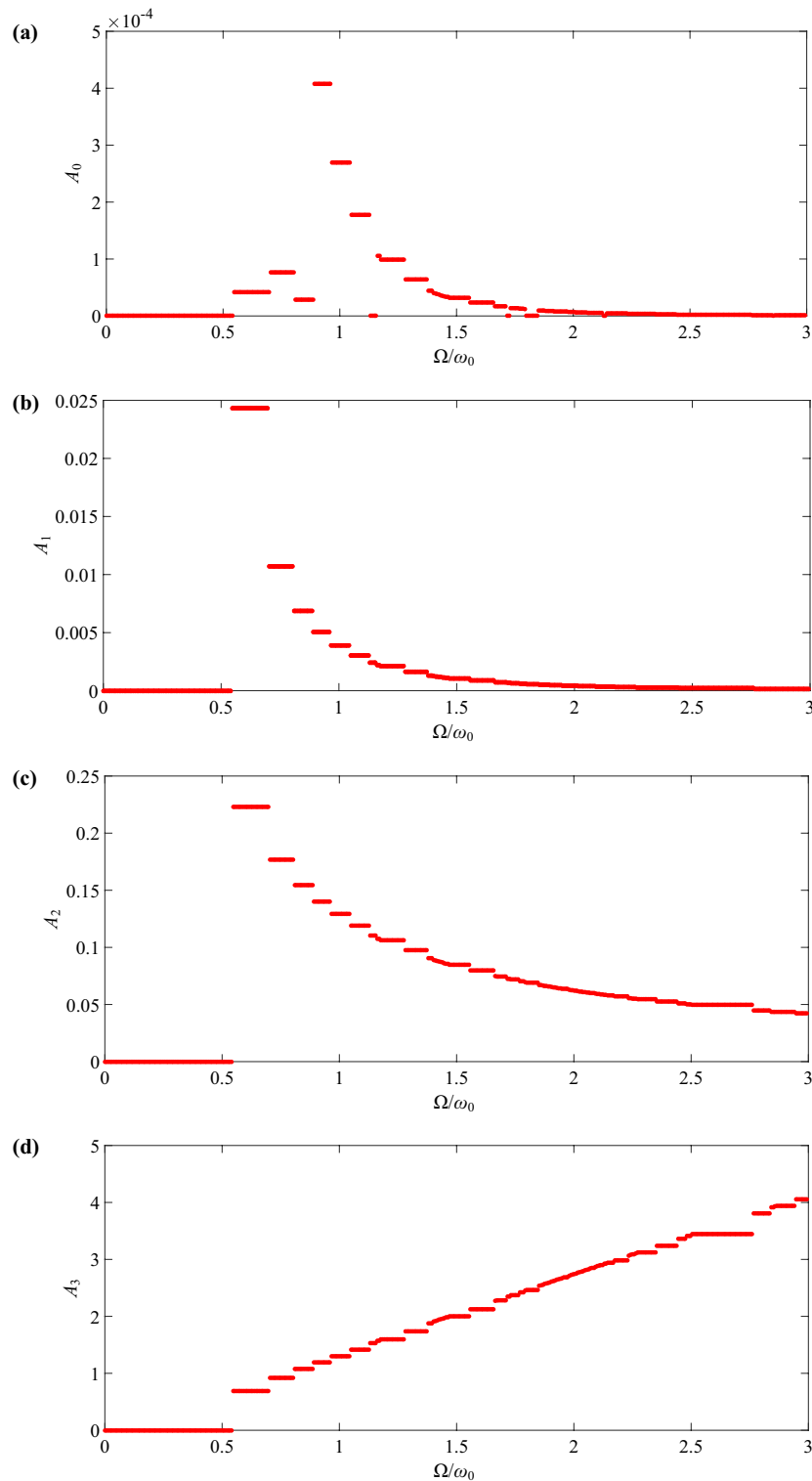


Fig. 13. Evolution curve of modal energy, where (a) First-order. (b) Second-order. (c) Third-order. (d) Fourth-order.

by the cell mapping theory is also able to reflect the energy transmigration of the nonlinear dynamical system. For dissipative dynamical systems with damping, the phase volume continuously shrinks during the motion of its solutions, i.e. $\text{div}V < 0$, where V denotes the phase volume. Moreover, it can be understood that any phase trajectory of a dissipative system will ultimately be attracted to a limit set with lower dimensions than the original space, namely an attractor, which represents the asymptotic behavior of the dynamic system when $t \rightarrow +\infty$. For

the dynamic system of nonlinear horizontal vibration for rolling mills, corresponding to any initial value, its trajectory or flow $\Gamma(t; x)$ can be expressed as:

$$\begin{cases} \Gamma(0; x) = x \\ \Gamma(s; \Gamma(t; x)) = \Gamma(t + s; x) \end{cases}$$

Assuming the set M_0 is the phase space at $t_0 = 0$, where x is a variable point, the corresponding flow can be plotted as shown in Fig. 14. At time t , the original set M_0 is moved and becomes the set $M_t = \Gamma(t; M_0)$. The calculation flowchart of the Cell Mapping Method is shown in Online Appendix Fig. 3.

In order to verify the energy orbit evolution characteristics of the steady-state response mode obtained by the homotopy analysis method, it is necessary to explore the attractor manifold variation characteristics of the system from the perspective of the energy transition of the oscillators during the nonlinear horizontal vibration process. By cell mapping theory, a generalized cell mapping dynamic system is constructed. Using the Poincaré section $\Sigma_0 = \{(x, dx/dt)\}$, Eq. (23) is simulated and analyzed, taking the systematic phase space as:

$$D = \{x \in [-1, 1], dx/dt \in [-2.5, 1.5]\}$$

Points of the ratio of excitation frequency to system frequency on different devil's staircase in Fig. 13a are selected as variables. Using the cell mapping method, the flow characteristics of systematic attractors and attraction domains is investigated, aiming to reveal the global motion characteristics of the roll's horizontal vibration system. Assuming a grid size of 100×100 cells, numerical simulation is conducted to obtain the systematic attractor and attraction domain when the frequency ratio Ω/ω_0 changes, as shown in Fig. 15.

As shown in Fig. 15a, when $\Omega/\omega_0 = 0.5$, there exists a periodic attractor A(1) in the phase space, corresponding to the systematic non-resonant solution, which is located in the attraction domain of a relatively large smooth boundary. As Ω/ω_0 increases to 0.56, from Fig. 15a,b, the system bifurcates, and the periodic attractor A(1) undergoes orbital transitions to form two attractors A(2) and A(3). The fingertips of the attractor collide with the boundaries of their respective attraction domains. At $\Omega/\omega_0 = 0.715$, attractors A(2) and A(3) expand in size, and the system exhibits increased chaotic behavior. Simultaneously, variations in the frequency ratio may lead to transitions of resonant solutions into attraction domains, eventually coexisting within the same attraction domain, as shown in Fig. 15c. When $\Omega/\omega_0 = 0.85$, the sizes of attractors A(2) and A(3) decrease, and the systematic chaos diminishes, as depicted in Fig. 15d. Additionally, it can be observed that as the frequency ratio increases, the manifold of attractors evolves, and fractal structures emerge around the attraction domains of the attractors. This indicates that increasing the frequency ratio not only destabilizes systematic periodic solutions but also reduces predictability. When $\Omega/\omega_0 = 0.9$, the systematic periodic attractor disappears, replaced by a large chaotic attractor A(4), which touches the boundaries of the attraction domains and occupies two attraction domains, as seen in Fig. 15e. This indicates that it may be extremely sensitive to small changes in operating conditions and the system is highly unstable. Figure 15f shows that as Ω/ω_0 continues to increase to 0.97, transient chaos weakens. When $\Omega/\omega_0 = 1.125$, oscillators with high energy in chaotic attractor A(4) undergo orbit transitions, forming attractor channels and initially developing into periodic attractors A(5), A(6), A(7), and A(8), each within their respective attraction domains. The attraction domains still exhibit entanglement phenomena, as depicted in Fig. 15g. According to chaos theory, when the system operates under extremely unstable conditions, the attractor enters a chaotic state. In such cases, the basin of attraction displays a highly diverse color pattern. This color diversity reflects the strong entanglement of the manifolds and their sensitivity to initial conditions, indicating that the system is in a highly unstable regime. From Fig. 15e.g, it is evident that due to the highly intertwined manifold of attractor's attraction domains, the systematic long-term response remains unpredictable, because it is not possible to determine at which iteration the chaotic attractor will occur in the presence of external perturbations. As Ω/ω_0 continues to increase, it is evident that with the movement and bifurcation of attractors, the corresponding structure of attraction domains changes. The system transitions from a period-4 attractor to a period-3 attractor, as shown in Fig. 15h. The boundaries of the attraction domains

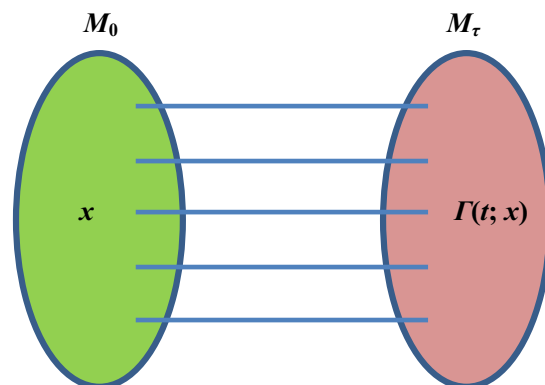


Fig. 14. Description of attractor flow.

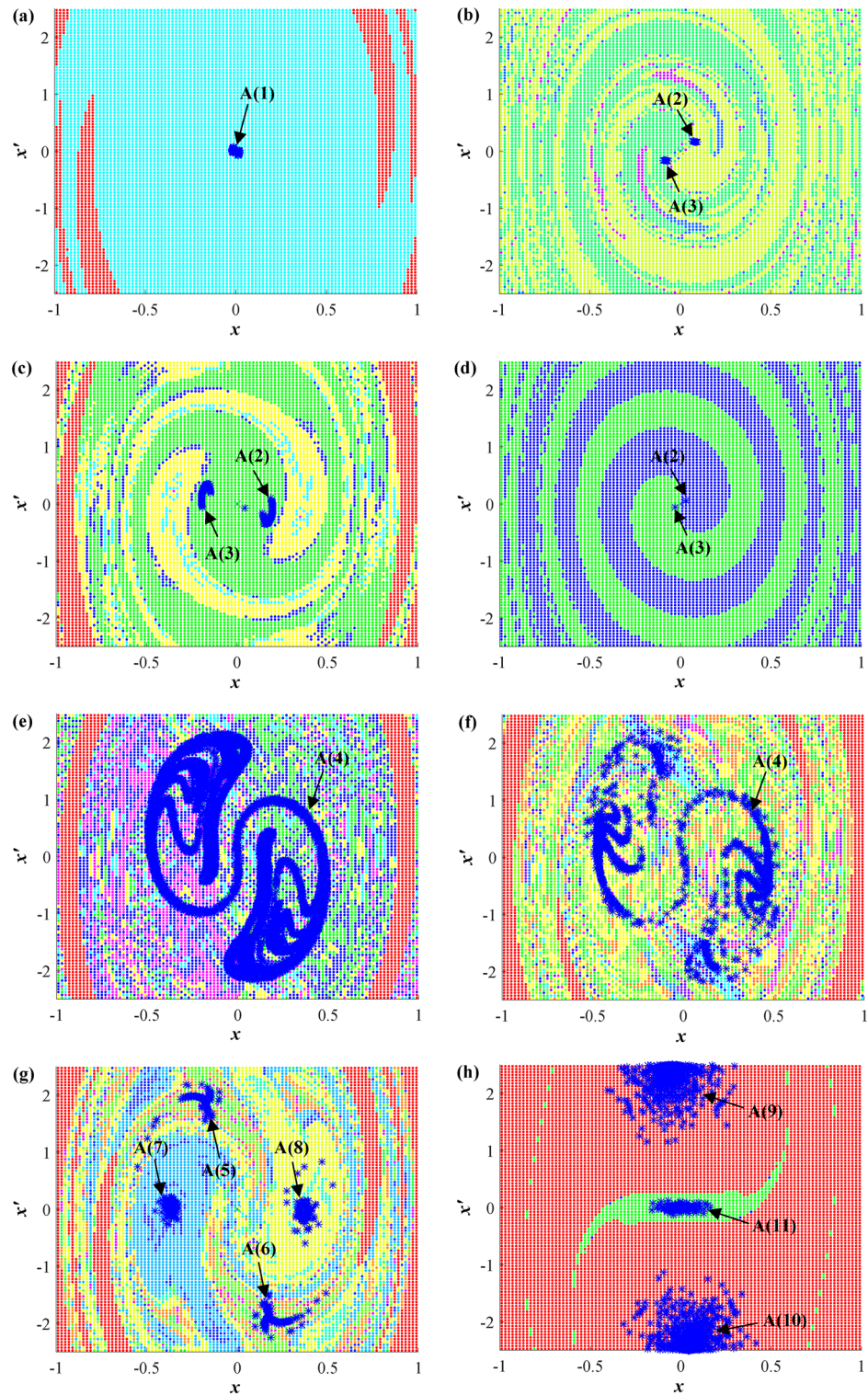


Fig. 15. Attractor and attraction domain diagram with frequency ratios Ω/ω_0 variation, where (a) $\Omega/\omega_0 = 0.5$. (b) $\Omega/\omega_0 = 0.56$. (c) $\Omega/\omega_0 = 0.715$. (d) $\Omega/\omega_0 = 0.85$. (e) $\Omega/\omega_0 = 0.9$. (f) $\Omega/\omega_0 = 0.97$. (g) $\Omega/\omega_0 = 1.125$. (h) $\Omega/\omega_0 = 1.25$.

become smooth, indicating that the system exhibits relative robustness to changes in initial conditions and minor disturbances, thereby enhancing stability.

In summary, considering the influence of axial excitation frequency, starting from the initial set of numerical solutions for the systematic horizontal vibration differential equations, the system undergoes a series of physical phenomena including attraction induction of periodic and chaotic attractors, ultimately converging to stable

fixed points. This indicates that changes in axial excitation frequency induce a transition between chaotic and periodic motion in the work roll's horizontal vibration system, and its essence is that the change of system energy promotes the manifold change of the oscillator group. The aforementioned analysis based on cell mapping theory shows that the influence of excitation frequency on the motion characteristics of attractors and attraction domains in the horizontal vibration system, as well as the mechanisms of system energy transition, are consistent with the evolutionary patterns of steady-state response of the first-mode shown in Fig. 13a. Therefore, the numerical solutions obtained based on the cell mapping theory provide validation to some extent for the analytical solutions obtained through homotopy analysis.

Construction of amplitude death conditions

Amplitude death refers to a state where the system's oscillations are entirely suppressed and stabilized to zero amplitude. In precision cold rolling operations, uncontrolled horizontal vibration of the work roll can lead to surface defects, thickness deviation, and unstable strip tension. Achieving amplitude death thus directly corresponds to eliminating unwanted oscillations, improving product quality, and enhancing equipment longevity.

It is well known that all system structures require a certain amount of runtime, which can cause control forces to lag. The time-delay control factor is introduced into the nonlinear vibration system to circumvent the control force hysteresis phenomenon by reasonably selecting the time-delay parameter. Therefore, time-delay control has become an effective method to suppress unfavorable vibrations in systems. In order to improve the complex nonlinear dynamic behavior of the above system to overcome the rolling instability induced by nonlinear factors, in this section, active damping and active stiffness bivariate time-delay control signals are introduced to the roll's horizontal vibration system under axial load excitation. The steady state response of a nonlinear horizontal vibration system is regulated and a stability control strategy for this fundamental physical problem is proposed.

When the control parameters are applied for systematic active control, i.e., g_1 , g_2 and τ are used as the control variables, the control mechanism for the nonlinear characteristics of the system is investigated by solving Eqs. (35) and (36). Let $da/dT_1 = d\varphi/dT_1 = 0$, and the equations on the amplitude a are obtained by simplification as follows

$$\frac{9}{4}k_3^2 a^4 - (12k_3\sigma\omega_0 + 6k_3g_1 \cos \tau + 6k_3g_2\omega_0 \sin \tau) a^2 + 4g_1^2 + 4g_2^2\omega_0^2 + 4c_1^2\omega_0^2 + 8c_1 (g_1\omega_0 \sin \tau - g_2\omega_0^2 \cos \tau) + 16\sigma^2\omega_0^2 + 16\sigma (g_1\omega_0 \cos \tau + g_2\omega_0^2 \sin \tau) - k_1^2 = 0 \quad (55)$$

$$\tan 2\varphi = \frac{-4c_1\omega_0 - 4g_1 \sin \tau + 4g_2\omega_0 \cos \tau}{8\sigma\omega_0 - 3k_3 a^2 + 4g_1 \cos \tau + 4g_2\omega_0 \sin \tau} \quad (56)$$

From Eq. (56), the amplitude expression can be obtained as

$$a_{1,2} = \sqrt{\frac{1}{3k_3} \left\{ 8\sigma\omega_0 + 4g_1 \cos \tau + 4g_2\omega_0 \sin \tau \pm \sqrt{(8\sigma\omega_0 + 4g_1 \cos \tau + 4g_2\omega_0 \sin \tau)^2 - 4[4g_1^2 + 4g_2^2\omega_0^2 + 4c_1^2\omega_0^2 + 8c_1 (g_1\omega_0 \sin \tau - g_2\omega_0^2 \cos \tau) + 16\sigma (g_1\omega_0 \cos \tau + g_2\omega_0^2 \sin \tau)]} \right\}} \quad (57)$$

In order to seek the matching combination of g_1 , g_2 and t_p , so that the parametric resonance corresponding to the maximum Arnold resonance tongue satisfies the amplitude death state, i.e., $a=0$. To set Eq. (57) equal to zero yields the condition for amplitude death as follows

$$g_1^2 + \omega_0^2 (g_2^2 + c_1^2 + 4\sigma^2) - \frac{k_1^2}{4} + 2c_1 (g_1\omega_0 \sin \tau - g_2\omega_0^2 \cos \tau) + 4\sigma (g_1\omega_0 \cos \tau + g_2\omega_0^2 \sin \tau) = 0 \quad (58)$$

Therefore, under specific systematic structural parameters, Eq. (58) can determine the relationship between control parameters and tuning parameter to achieve amplitude death in the horizontal vibration system, so as to control the systematic operational stability.

From Fig. 16, when the damping and excitation stiffness are selected, the change of the time delay τ leads to the counterclockwise rotation of the σ - g_2 solution curve around the center point, which can change the system frequency value in a small range when it meets the amplitude death. The change of displacement gain g_1 causes the solution curve to shift to the left, which can significantly change the frequency value to satisfy the systematic amplitude death. Simultaneously adjusting both the time delay τ and the displacement gain g_1 will cause the solution curve to shift to the left and rotate counterclockwise.

In order to more intuitively analyze the relationship between different combinations of control parameters and tuning frequency, a set of control parameter constraints was constructed for different tuning frequencies. Below, taking two control parameters as continuous variables, a three-dimensional solution surface of tuning parameters versus control parameters are obtained through simulation, as shown in Fig. 17.

Figure 17 shows three-dimensional relationship surfaces of the velocity gain g_2 versus tuning parameter σ and displacement gain g_1 , displacement gain g_1 versus tuning parameter σ and time-delay τ , and velocity gain g_2 versus tuning parameter σ and time-delay τ . The curve shown in Fig. 16 is the cross-section of the three-dimensional surface in Fig. 17. From Fig. 17a, it can be seen that when the time-delay τ takes a constant value, the surface map presents an elliptical cylindrical shape and no torsional deformation occurs. From Fig. 17b,c, it can be seen that the variation of the time-delay τ leads to a spatial twisting and deformation of the 3D solution

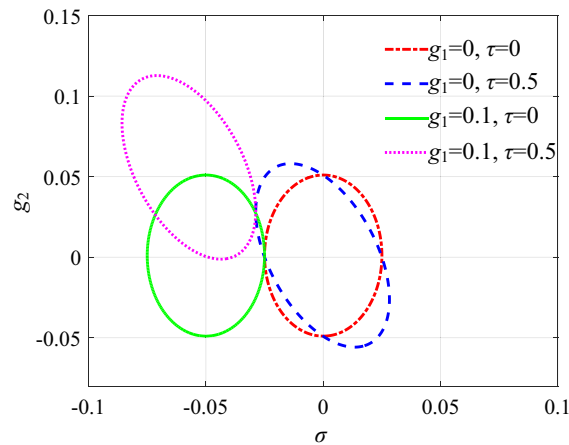


Fig. 16. Solution curve of σ - g_2 under different displacement gain and time delay.

surface map, which exhibits a certain periodicity. Based on the three-dimensional surface plots (see Fig. 17) and its two-dimensional cross-sections (see Fig. 16), the selection of regulation parameters on the surface map can make the system satisfy the amplitude death state. Thus, the set of points on the surface constitutes the corresponding set of control parameter constraints when the system satisfies the amplitude dead state, which can effectively weaken the above complex nonlinear behavior exhibited by the system.

The Figs. 16 and 17 collectively serve as a parametric sweep for evaluating the robustness of the amplitude-death condition. The Fig. 17 presents the cross-sectional solution curves under different combinations of displacement gain g_1 , velocity gain g_2 , and time-delay τ , showing how each parameter influences the location of amplitude death. The Fig. 17 further extends this analysis by constructing three-dimensional solution surfaces in the σ - g_1 - g_2 , σ - τ - g_1 , and σ - τ - g_2 spaces. These surfaces clearly identify the regions in the parameter space where the amplitude of the system response approaches zero.

This parametric investigation reveals that the amplitude-death phenomenon is not limited to a single operating point but is achievable across a broad range of control parameter combinations. Therefore, the proposed time-delay control strategy demonstrates strong robustness in suppressing undesirable nonlinear vibrations under various system conditions.

Conclusion

The results of the study constitute an evaluation mechanism for stabilizing and controlling the implicit dynamic characteristics of the precision cold rolling system, which further provides a theoretical reference for rolling processing and control. The main conclusions are as follows:

- (1) By multi-scale method, the amplitude-frequency characteristics of the primary parameter resonance corresponding to the maximum Arnold resonance tongue were analyzed to obtain the steady-state response curve. The results show that as the tuning frequency σ increases, the response amplitude firstly increases and then decreases, and when $\sigma=0$, the response amplitude is maximum, and resonance phenomenon occurs. In this case, the system will experience two catastrophic bifurcation points. In addition, comparing the amplitude response paths when increasing and decreasing σ , it is found that the system has different resonance behaviors with hysteresis characteristics, which are caused by the presence of multiple coexisting nontrivial solutions.
- (2) The homotopy analysis method is used to solve the energy orbit curves of each order mode for the roll's horizontal vibration system. The research results show that the first-mode amplitude is basically consistent with the steady-state response obtained by the multi-scale method. In addition, it is found that there are bifurcation and nonlinear discontinuous jumping characteristics with devil's staircase pattern, exhibiting multiple locked-frequency regions. Based on the discontinuous jump characteristic, the excitation frequency can be adjusted under actual working conditions of the rolling mill to broaden its corresponding locked-frequency region that is conducive to system stability, and to constrain the systematic complex dynamic behavior from an energy perspective.
- (3) By the cell mapping theory, the influence of excitation frequency on the manifold changes of attractors and attraction domains under multiple initial conditions is studied. It is found that as the excitation frequency increased, multiple attractors coexisted, and the system undergoes the transition from single-period attractors, multi period attractors, chaotic attractors and finally to multi-period attractors, which corresponds to the systematic steady-unstable-stable state of motion. Therefore, the energy orbit evolution characteristics of the steady-state response analyzed by the homotopy analysis method are verified through the manifold changes of oscillator group energy, revealing the evolution mechanism of the systematic dynamic behavior from a global perspective.
- (4) Through the time-delay control theory analysis, the constraint set of control parameters is constructed to satisfy the systematic amplitude death in the maximum Arnold resonance tongue region. The results show,

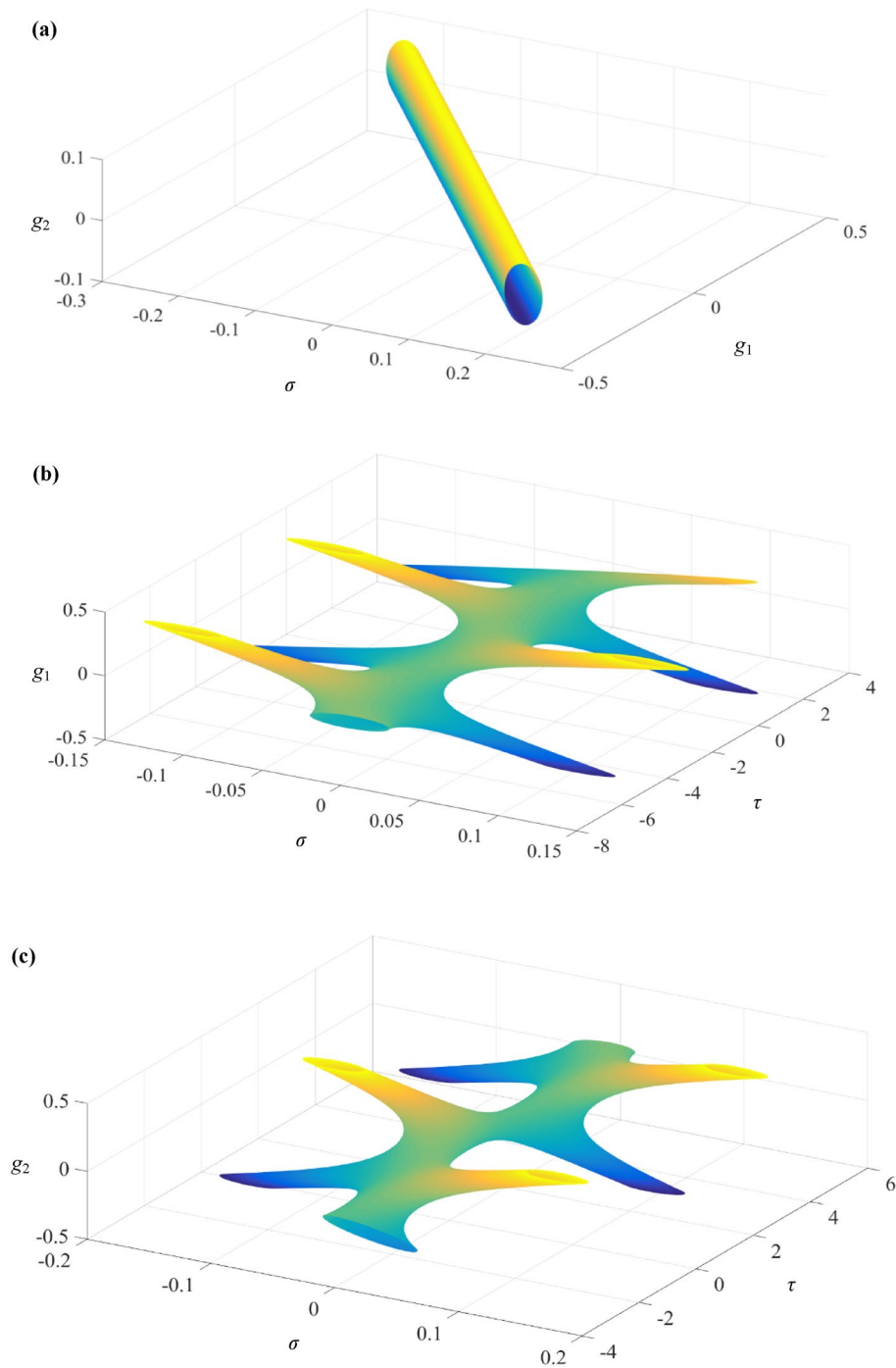


Fig. 17. 3D plots of frequency σ against control parameters, where (a) σ - g_1 - g_2 , (b) σ - τ - g_1 , (c) σ - τ - g_2 .

the gains of displacement and velocity can significantly alter the frequency of the resonance instability region, while time delay can periodically alter the matching relationship between gains and frequency. The above complex nonlinear characteristics of the vibration system are improved by active regulation of the control parameters to overcome the rolling instability induced by nonlinear factors.

- (5) While the proposed model offers a detailed theoretical framework for understanding and controlling roll-induced horizontal vibrations, it is sensitive to parameter variations—such as stiffness, damping, time delay, and excitation frequency—which significantly influence the systematic dynamic response. Future studies may expand the model to address non-stationary rolling conditions, including time-varying speeds and multi-directional coupled vibrations. Furthermore, the proposed control strategy can be adapted for real-time implementation, and may serve as a foundation for developing digital twin systems to enable predictive diagnostics and intelligent optimization in modern rolling mills.

In summary, by analyzing the stability and control mechanisms of horizontal vibrations in a precision four-high cold rolling mill, this study elucidates the underlying dynamics governing system motion paths under axial excitation. It further reveals the relationship between excitation frequency and the stability of horizontal vibrations. Moreover, the control mechanism necessary to induce amplitude death under gyroscopic effects is established. These findings provide a theoretical foundation for enhancing operational stability and ensuring dynamic reliability in high-precision rolling systems.

Data availability

The data that support the findings of this study are available from the corresponding author upon reasonable request.

Received: 5 July 2024; Accepted: 4 November 2025

Published online: 27 November 2025

References

- Xu, H., Ren, C. & He, D. Coupling vibration characteristics and vibration suppression of rolling mill rolls with dynamic vibration absorber. *J. Manuf. Process.* **120**, 1157–1179 (2024).
- Zhu, Y. & Qian, P. F. Amplitude-frequency characteristics analysis for vertical vibration of hydraulic AGC system under nonlinear action. *AIP Adv.* **9**(3), 035019 (2019).
- He, D. P. & Xu, H. D. Nonlinear time-delay feedback controllability for vertical parametrically excited vibration of roll system in corrugated rolling mill. *Metall. Res. Technol.* **117**(2), 210 (2020).
- Zhang, Y. S. & Jiang, W. L. Research on the vertical vibration characteristics of hydraulic screw down system of rolling mill under nonlinear friction. *Processes.* **7**(11), 792 (2019).
- Zhao, W., Liu, B. & Jiang, J. S. Analysis and calculation of rolling mill torsional vibration based on topological network. *J. Mech. Eng.* **07**, 51–55 (2006).
- Liu, S. & Liu, J. J. Bifurcation control for electromechanical coupling torsional vibration in rolling mill system driven by DC motor. *Int. J. Appl. Electrom.* **50**(1), 113–125 (2016).
- Liu, S. & Ai, H. L. Bifurcation and chaos of electromechanical coupling main drive system with strongly nonlinear characteristic in mill. *Chaos. Soliton. Fract.* **98**, 101–108 (2017).
- Zhang, R. C., Zhang, S. Q. & Liang, W. Z. Study on horizontal vibration for rolling mill under influences of harmonic moment and roll system eccentricity. *Forg. Technol.* **48**(10), 182–191 (2023).
- Shen, G. X. & Li, M. Statically determinate characteristics of micro-displacement in a four-high mill. *J. Mater. Process. Tech.* **209**(11), 5002–5007 (2009).
- Sun, C. F., Zhao, W. & Huang, D. Stability of nonlinear vibrations induced by rolling force in a precise cold mill system. *Appl. Math. Model.* **119**, 196–217 (2023).
- Wang, X. X. & Yan, X. Q. Dynamic model of the hot strip rolling mill vibration resulting from entry thickness deviation and its dynamic characteristics. *Math. Probl. Eng.* **2019**, 5868740 (2019).
- Yan, X. Q. & Qi, J. B. An active method suppressing rolling mill vibration: disturbance estimation and compensation algorithm. *J. Iron. Steel. Res. Int.* **26**(7), 697–703 (2019).
- Cui, J. X., Peng, Y. & Wang, J. Instability of roll nonlinear system with structural clearance in rolling process. *J. Iron. Steel. Res. Int.* **30**(1), 112–125 (2023).
- Liu, Z. L. & Jiang, J. H. Dynamic analysis and control of strip mill vibration under the coupling effect of roll and rolled piece. *J. Vibroeng.* **19**(8), 6079–6093 (2017).
- Liu, B. & Jiang, J. H. Nonlinear vibration characteristic of strip mill under the coupling effect of roll-rolled piece. *J. Vibroeng.* **18**(8), 5492–5505 (2016).
- Jiang, L., Yang, T., Shi, W. & Xie, J. Q. Research on horizontal nonlinear sub-harmonic vibration characteristics and stability control of rolling mill roll system. *Sci. Rep.* **15**(1), 22420 (2025).
- Jiang, L., Wang, T. & Huang, Q. X. Resonance analysis of horizontal nonlinear vibrations of roll systems for cold rolling mills under double-frequency excitations. *Mathematics.* **11**(7), 1626 (2023).
- Cui, Z. J., Zhang, X. R. & Lu, T. Resonance analysis and time-delay feedback controllability for a fractional horizontal nonlinear roller system. *Aims. Math.* **9**(9), 24832–24853 (2024).
- Zhou, J. L. et al. Horizontal vibration of a single-roll driven cold rolling temper mill. *J. Wuhan Univ. Sci. Tech.* **42**(3), 174–181 (2019).
- Zhao, H. Y. & Kornel, F. E. Stability analysis of chatter in tandem rolling mills-part 1: Single- and multi-stand negative damping effect. *J. Manuf. Sci. E-T. ASME.* **135**(3), 031001 (2013).
- Kazushige, I. & Kazuhisa, K. Vibration analysis of chatter in cold rolling mill. *Trans. Jpn. Soc. Mech. Eng. Ser. C* **69**(695), 1906–1913 (2003).
- Li, L. & Hao, Y. C. A study on horizontal vibration characteristics of cold rolling mill's work roll under combined excitation. *J. Vib. Shock.* **41**(16), 135–141 (2022).
- Liu, B. & Jiang, J. H. Nonlinear vibration characteristics of strip mill influenced by horizontal vibration of rolled piece. *Chin. Mech. Eng.* **27**(18), 2513–2520 (2016).
- Shen, G. & Yu, C. Mechanism generating deviations in the rolling load and strip camber on the plate rolling mill. *Iron. Steel.* **44**(9), 707–711 (2017).
- Li, M. *Study of Micro-Dimensional Dynamic Cross Behavior Mechanism of Four-High Mill and Its Control Method.* (Yanshan University, 2004).
- Fan, X. B. Impact analysis of roller system stability for four-high mill horizontal vibration. *Shock Vib.* **2016**, 5693584 (2016).
- Zheng, Y. J. & Shen, G. X. Spatial vibration and its numerical analytical method of four-high rolling mills. *J. Iron. Steel. Res. Int.* **21**(9), 837–843 (2014).
- Sun, C. F. et al. Nonlinear dynamics and stability analysis of horizontal vibration for rolling system with gyroscope precession and eccentricity effects. *Alex. Eng. J.* **124**, 303–316 (2025).
- He, D. P. et al. Horizontal nonlinear vibration of mill work roll and intelligent liner vibration absorption. *J. Mech. Eng.* **60**(20), 108–119 (2024).
- Chen, J. Q. et al. Robust low-complexity vibration suppression control of rolling mill with time-varying state constraints. *Int. J. Syst. Sci.* **56**(5), 1081–1094 (2025).
- Li, X. Y., Wang, X. H. & Chen, Y. Y. Bending, buckling and free vibration of an axially loaded Timoshenko beam with transition parameter: Direction of axial force. *Int. J. Mech. Sci.* **176**, 105545 (2020).
- Ma, W. L., Cheng, C. & Chen, X. Free vibration of radially graded hollow cylinders subject to axial force via a higher-order shear deformation beam theory. *Compos. Struct.* **255**, 112957 (2021).

33. Yousef, S. A. R. & Azhar, G. H. Forced vibration of axially-loaded, multi-cracked Euler-Bernoulli and Timoshenko beams-ScienceDirect. *Structures*. **25**, 370–385 (2020).
34. Huang, Y. & Chang, K. Stability analysis of a rotating beam under a moving motion-dependent force. *J. Sound Vib.* **202**, 427–437 (1997).
35. Kovacic, I., Rand, R. & Sah, S. Mathieu's equation and its generalizations: Overview of stability charts and their features. *Appl. Mech. Rev.* **70**(2), 020802 (2018).
36. Atanasov, M. & Stojanovi, V. Nonlocal forced vibrations of rotating cantilever nano-beams. *Euro. J Mech.-A/Solids* **79**, 103850 (2019).
37. Wang, L., Zhao, Y. & Zhu, Q. Nonlinear vibration characteristic analysis of roller-plate system based on asymptotic methods. *ISIJ. Int.* **60**(6), 1237–1244 (2020).
38. Liao, S. J. A kind of approximate solution technique which does not depend upon small parameters: A special example. *Int. J. Nonlin. Mech.* **30**(3), 371–380 (1995).

Acknowledgements

This work was supported by the Joint Funds of Doctoral Special Fund Project of Nanyang Normal University (Grant No. 2024ZX029); the National Natural Science Foundation of China (Grant No. U1604140); the Key Research Project of Higher Education Institutions of Henan Province (Grant No. 25A460003); the Key Science and Technology Program of Henan Province, China (Grant Nos. 172102210269, 192102210052, 212102210108, 212102210004); the Major Achievements Cultivation Project of Henan Province, China (Grant No. NSFRF170503); the Key Scientific and Technological Project of Henan Province (Grant No. 232102211047); Doctoral Special Fund Project of Nanyang Normal University (Grant No. 2020ZX009); Youth Fund Project of Natural Science Foundation of Henan Province (Grant No. 242300421464); Doctoral Special Fund Project of Nanyang Normal University (Grant No. 2024ZX025); Cultivation Project of National Natural Science Foundation of Nanyang Normal University (Grant Nos. 2024PY023, 2023PY011).

Author contributions

Chaofan Sun wrote the main manuscript text, also including data curation, formal analysis, software, visualization, funding acquisition. Wu Zhao: the main work is focused on conceptualization, methodology, writing-review & editing, validation, funding acquisition. Wei Liu: the main work is focused on supervision, project administration, funding acquisition. Guiquan Han: the main work is focused on investigation, validation, funding acquisition. Yuqi Chen: the main work is focused on validation, funding acquisition. Junyang Duan: the main work is focused on writing-review & editing, visualization, validation. All authors reviewed the manuscript.

Declarations

Competing interests

The authors declare no competing interests.

Additional information

Supplementary Information The online version contains supplementary material available at <https://doi.org/10.1038/s41598-025-27552-2>.

Correspondence and requests for materials should be addressed to C.S.

Reprints and permissions information is available at www.nature.com/reprints.

Publisher's note Springer Nature remains neutral with regard to jurisdictional claims in published maps and institutional affiliations.

Open Access This article is licensed under a Creative Commons Attribution-NonCommercial-NoDerivatives 4.0 International License, which permits any non-commercial use, sharing, distribution and reproduction in any medium or format, as long as you give appropriate credit to the original author(s) and the source, provide a link to the Creative Commons licence, and indicate if you modified the licensed material. You do not have permission under this licence to share adapted material derived from this article or parts of it. The images or other third party material in this article are included in the article's Creative Commons licence, unless indicated otherwise in a credit line to the material. If material is not included in the article's Creative Commons licence and your intended use is not permitted by statutory regulation or exceeds the permitted use, you will need to obtain permission directly from the copyright holder. To view a copy of this licence, visit <http://creativecommons.org/licenses/by-nc-nd/4.0/>.

© The Author(s) 2025